

## Electrically Tunable Heliconical Smectic Superstructure in Polar Fluids

Hiroya Nishikawa<sup>\*,1</sup>, Dennis Kwaria<sup>1</sup>, Atsuko Nihonyanagi<sup>1</sup>, Koki Sano<sup>2</sup>, Hiroyuki Yoshida<sup>3</sup> and Fumito Araoka<sup>\*,1</sup>

<sup>1</sup> RIKEN Center for Emergent Matter Science, 2-1 Hirosawa, Wako, Saitama 351-0198, Japan

<sup>2</sup> Department of Chemistry and Materials, Faculty of Textile Science and Technology, Shinshu University, 3-15-1 Tokida, Ueda, Nagano 386-8567, Japan

<sup>3</sup> School of Engineering, Kwansei Gakuin University, 1 Gakuen Uegahara, Sanda, Hyogo 669-1330, Japan

E-mail: hiroya.nishikawa@riken.jp; fumito.araoaka@riken.jp

### Abstract

The groundbreaking discovery of the ferroelectric nematic ( $N_F$ ) phase has attracted broad interest owing to its pronounced polarization properties and high fluidity. Building on this, the emergent spontaneous chiral order in achiral molecular systems, such as the heliconical ferroelectric nematic phase ( $N_{TBF}$ ) and the polar heliconical smectic C phase ( $SmC_P^H$ ), has been discovered, revealing a new form in hierarchical polar order: hierarchical symmetry breaking. Here we report a newly designed achiral molecule that exhibits a hierarchical polar phase sequence: ferroelectric smectic A– $N_{TBF}$ –helielectric conical– $SmC_P^H$  phases. We confirm that the  $SmC_P^H$  phase can form a stable macroscopic orientation under an electric field, without any alignment layer. Remarkably, we unlock the unprecedented functionality of the  $SmC_P^H$  phase: ultralow-voltage and low-frequency-driven modulation of the helical pitch and its associated enhanced second-harmonic generation. These results demonstrate emergent functionality of polar fluids arising from hierarchical symmetry breaking and offering a new paradigm for polar soft-matter photonics.

### 1. Introduction

A distinct state of fluid matter characterized by ferroelectric order, the ferroelectric nematic liquid crystal ( $N_{FLC}$ )[1–3], has garnered enormous attention within the broad scientific community. In the  $N_F$  phase, the head–tail symmetry of the local director ( $\mathbf{n} = -\mathbf{n}$ ) present in a uniaxial nematic (N, **Figure 1a**) phase is lifted, allowing the emergence of a polar structure ( $\mathbf{n} \neq -\mathbf{n}$ ,  $\mathbf{n} \parallel \mathbf{P}$ , where  $\mathbf{P}$  is the polarization vector) (Figure 1b). This structural property of the  $N_F$  phase offers remarkable polarization characteristics—such as large polarization density and

a strong nonlinear optical response—and simultaneously maintains high fluidity.[4] Therefore, the  $N_F$  phase is an extremely interesting subject not only from a fundamental scientific perspective but also for potential new device applications.[5] To date, diverse hierarchical polar phases have emerged when smectic-layer order[6–9] or induced [10–12]/spontaneous [13,7,14] chiral order is introduced starting from the  $N_F$  phase. These novel polar LC phases, unlike the uniaxial polar order exhibited by  $N_F$  phases, are characterized by concerted order formation between molecular-scale dipole alignments and mesoscale structures. Hence, they update definition of the polar LC science paradigm regarding the coexistence of polar order and fluidity, and are expected to lead to the establishment of new design principles for translating molecular order into functional expression.

When smectic-type layer order emerges from the  $N_F$  phase, a ferroelectric smectic A ( $SmA_F$ ) phase[6–8] appears (Figure 1c). This phase is a polar version of the orthogonal smectic A phase and, similar to the  $N_F$  phase, possesses a lamellar structure ( $\mathbf{n} \parallel \mathbf{P}$ ). Furthermore, when molecules within the  $SmA_F$  phase layer tilt, a hierarchical structural phase transition occurs to the ferroelectric smectic C ( $SmC_F$ ) phase.[15,8,16] Both phases exhibit proper ferroelectric response because  $\mathbf{n}$  and  $\mathbf{P}$  simultaneously reverse upon polarity inversion of the electric ( $E$ -) field, thereby enabling bistable in-plane polarization memory functionality.[17,18,15] The chiral nematic ( $N^*$ ) phase, with its helicoidal structure, is formed by induced chirality derived from the intrinsic asymmetry of chiral dopants or chiral mesogens.[19] Recently, a chiral ferroelectric nematic ( $N_F^*$ ) phase has been experimentally and theoretically confirmed by designing chiral polar molecules[20,21] or by doping chiral dopants[10,11] into the  $N_F$  phase. In the  $N_F^*$  phase, inversion symmetry is broken, whereas chirality is intrinsically determined. Unlike conventional  $N^*$  phases, the  $N_F^*$  phase exhibits a unique functionality—when an  $E$ -field is applied perpendicular to its helical axis, it enables rapid switching between half-to full-pitch helicoidal state owing to the strong coupling between the polarization and  $E$ -field. [10]

Another notable development is the discovery of the new polar helielectric phases, namely the heliconical ferroelectric nematic ( $N_{TBF}$ ) (Figure 1d) [13,7] and the polar heliconical smectic ( $SmC_P^H$ , HEC) (Figure 1e) phases,[22,23] each of which exhibits a heliconical structure that spontaneously arises from the achiral molecules through the spontaneous chiral symmetry breaking. These represent novel helielectric phases characterized by “hierarchical symmetry breaking,” where inversion symmetry is broken first, followed by chiral symmetry breaking. For the  $N_F^*$  and  $N_{TBF}$  phases, where the pitch lies within the visible light range, applications in photonic materials—such as color modulation by electrostimuli or photostimuli[24] and laser oscillation[25,26]—have been reported. However, the  $SmC_P^H$  phase primarily responds to

control of the helical axis,[23] and the development of its functionality and utility as photonic materials remains unexplored.

In this study, based on the previously reported polar molecule (Model I , **Figure 2a**) exhibiting the polar heliconical (HEC) phase (Figure 1a),[27] we designed a new Model II (Compound **1**, Figure 2b) by introducing an additional fluorine atom into the aromatic ring proximal to the alkyl chain of Model I. Polar molecules with such a structure bearing alkyl ester units can be synthesized more easily than the conventional derivatives with 1,3-dioxane moieties and typically, exhibit superior thermal stability. Therefore, alkyl ester variants offer high utility for facilitating easier and more multifaceted evaluation of emergent ferroelectricity. The results revealed that Compound **1** exhibits a phase transition sequence based on hierarchical symmetry breaking:  $N-N_x-SmA_F-N_{TBF}-HEC-SmC_p^H$ , upon cooling. Notably, the  $SmC_p^H$  phase of this molecule exhibits a polar helielectric lamellar structure, whose optical full pitch lies within the visible light wavelength range and can be uniformly orientated by an *E*-field. Since such a  $SmC_p^H$  phase with a superior electro-optic property has not been reported previously, the present study aims at demonstrating its functionality. Particularly, ultralow-voltage reflective color modulation and amplified second harmonic generation (SHG) associated with it were successfully achieved for the first time.

## 2. Results and Discussion

### 2.1. Phase transition behavior

The differential scanning calorimetry (DSC) curve (Figure 2c; Figure S1, Supporting Information) and polarized optical microscopy (POM) images of Compound **1** (Figure 2d–s; Figure S2, Supporting Information) were used to characterize its phase transition behavior. For POM studies, we used syn-parallel rubbing polyimide (SP) glass cells (Figure 2d–h), bare substrate cells (Figure 2i–m), and indium tin oxide (ITO)-coated glass cells (Figure 2n–s). In the SP cell, cooling from the nematic (N) phase caused many defects to appear along the rubbing direction (Figure S2b, Supporting Information), which then developed into uniform block-like domains aligned in the rubbing direction (Figure 2d). These features are typical in the  $N_x$  [28] or  $N_F$  phase transiting into the  $SmA_F$  phase. We hereinafter refer to this as the  $N_x$  phase since it exhibited an antiferroelectric-like electrical response (Figure S12, Supporting Information). Further cooling revealed a stripe texture along the rubbed direction, with additional finer stripes appearing perpendicular to the initial stripes (Figure 2e). Within this temperature range, colored reflection or scattering was visible in the LC cell. This was more obvious in a bare substrate cell (Figure 2j). This color was likely due to the selective reflection, and hence the phase was

assigned to the  $N_{TBF}$  phase, which forms a polar heliconical structure generated to reduce the electrostatic potential under mediation of the elastic effects. The full pitch of the fine stripes corresponds to that of the heliconical structure, which was estimated to be  $\approx 1.3 \mu\text{m}$  (Figure S3, Supporting Information). It is noteworthy to mention that Strachan et al. discussed the possible competition of the  $\text{SmA}_F$  and  $N_{TBF}$  phases [29], and that no  $N_{TBF}$ – $\text{SmA}_F$  phase transition within a single molecule has yet been reported to date. The  $N_x$ – $\text{SmA}_F$ – $N_{TBF}$  phase transition in Compound **1** is obviously one of the rare examples of the reentrant phenomenon in polar phases [9], where the restoration of nematic order follows the collapse of smectic layer order, although the mechanism of this is not yet unclear. The  $N_{TBF}$  phase existed only within a narrow temperature range of approximately 1 K, after which inhomogeneous textures of the HEC phase appeared (Figure 2e,f; Figure S4a–c, Supporting Information). Such a textural change was also observed in thicker/thinner bare substrate (Figure j–l; Figure S4d–f, Supporting Information) and thinner ITO cells (Figure S4g–h, Supporting Information). Interestingly, in the bare substrate cell, a spiraling-filament-like texture was observed in the same temperature region (Figure 2k and 2l). The similar spiraling filaments were also observed in the HEC phase in our previous study. [27] In the SP cell, the faint reflective color was red-shifted upon cooling, and eventually the texture transited into a darker state at  $84^\circ\text{C}$  (Figure 2g, 2h; Figure S2f–l, Supporting Information). A texture with low birefringence was also observed at  $85^\circ\text{C}$  in the bare substrate cell (Figure 2m). The ITO-coated cell within this temperature range displayed sub-millimeter-sized island domains in which the contrast between adjacent domains was reversed by decrossing the polarizers in the opposite directions, indicating optical activity (Figure 2n–p). Furthermore, reflection microscopy confirmed reflective colors (Figure 2q–s) of left- or right-handed circularly polarized selective reflection. Given the generation of enantiomeric domains and the observation of selective reflective color, this phase under the HEC phase was speculated to be the  $\text{SmC}_P^H$  phase. So far, the control over both the reflective color and the orientation of the helical axis in the  $\text{SmC}_P^H$  phase is yet difficult [22,23]. In contrast, the  $\text{SmC}_P^H$  phase in Compound **1** enables both *E*-field-induced reorientation of the helical axis and color modulation via the helical pitch variation, as will be demonstrated in the below.

## 2.2. Structural characterization

Two-dimensional (2D) wide-angle X-ray diffraction (XRD) patterns were obtained for structural characterization of Compound **1** at various temperatures (Figure 3a–d; Figure S5–S6, Supporting Information). The corresponding 1D XRD plots were generated by the box scan analysis (Figure S7, Supporting Information) along the equator parallel to the applied magnetic field **B** ( $\mathbf{n} \parallel \mathbf{B}$ ) of the 2D XRD pattern (Figure 3e, f; Figure S8, Supporting Information). The

following parameters were then obtained as functions of temperature:  $d$ -spacing ( $d = 2\pi/q$ ) (Figure 3g), tilt angles ( $\theta_{\text{tilt}}$ ) (Figure 3g), full width at half maximum (FWHM) of the scattering vector,  $q$  ( $\Delta q_{\text{FWHM}}$ ) (Figure 3h), and the peak intensity (Figure 3h). The diffraction pattern of the N phase can be attributed to short-range positional ordering of molecules along **B** (Figure S6a, Supporting Information). Although the peak intensities and positions were almost the same in the N and  $N_x$  phases (Figure S6b, Supporting Information),  $\Delta q_{\text{FWHM}}$  was smaller in the  $N_x$  phase than in the N phase. After the transition to the SmA<sub>F</sub> phase, the diffraction peak became sharper, and  $\Delta q_{\text{FWHM}}$  was greatly reduced, suggesting an increase in the correlation length. In the SmA<sub>F</sub> phase,  $d$  became almost consistent with the molecular length ( $L$ ) due to the formation of the non-tilted lamellar structure. After transition to the  $N_{\text{TBF}}$  and HEC phases, the diffraction pattern became an ark-like shape which is typical in the helielectric phases. Within the HEC phase temperature range,  $d$  gradually decreased upon cooling, meaning that the molecules in the lamellar were tilted with respect to the layer normal. The molecular tilting started at the lower-temperature side of the SmA<sub>F</sub> phase, with the tilt angle measured as  $2^\circ < \theta_{\text{tilt}} < 7^\circ$  where  $\theta_{\text{tilt}} = \arccos(\frac{d}{L})$ . Peak intensity,  $d$  and  $\Delta q_{\text{FWHM}}$  jump at the HEC–SmC<sub>P</sub><sup>H</sup> phase transition, suggesting the first-order type. In the SmC<sub>P</sub><sup>H</sup> phase, the molecular orientation with respect to the magnetic field deviated substantially. The SmC<sub>P</sub><sup>H</sup> phase exhibited further gradual reduction in  $d$ , leading to a maximum tilt angle  $\theta_{\text{tilt}} = 21^\circ$ , despite an almost constant  $\Delta q_{\text{FWHM}}$ . On the other hand, in the HEC phase,  $\Delta q_{\text{FWHM}}$  increased and then reached a plateau. This suggests that, although both the HEC and SmC<sub>P</sub><sup>H</sup> phases possess polar heliconical ordering of the tilted smectics, the coherence of the structure in the HEC phase was reduced upon cooling, implying the generation of small fragments or clusters of the smectic ordering.

### 2.3. Polar behavior

Next, the polar behavior of various phases was evaluated using broadband dielectric spectroscopy (BDS), polarization reversal current (PRC) and second harmonic generation (SHG) measurements. As shown in **Figure 4a–c** and Figures S9 and S10 (Supporting Information), the BDS results revealed that the apparent dielectric permittivity ( $\epsilon'_{app}$ ) increased to  $\approx 5k$  at the N– $N_x$  phase transition point, decreased sharply to a minimum of  $\approx 0.4k$  in the SmA<sub>F</sub> phase, and recovered to  $\epsilon'_{app}$  of  $\approx 10k$  in the  $N_{\text{TBF}}$  phase. This sequence of permittivity changes is likely attributed to the suppression of polarization fluctuations [8] and the restoration of a strong collective relaxation mode [30,13] in the SmA<sub>F</sub> and  $N_{\text{TBF}}$  phases, respectively (Figure 4b). In the HEC phase,  $\epsilon'_{app}$  remained  $\approx 10k$  in the high-temperature region but gradually decreased toward the low-temperature region, reaching a plateau at approximately 3k. Upon the

phase transition from the HEC phase to the  $\text{SmC}_\text{P}^\text{H}$  phase, the dielectric permittivity recovered to  $\approx 7.6\text{k}$  and then gradually decreased to  $\approx 1.7\text{k}$ . As confirmed by XRD measurements, molecules in the HEC and  $\text{SmC}_\text{P}^\text{H}$  phases exhibited the tilted smectic ordering, suggesting that both correspond to the processional Goldstone mode on the tilt cone (Figure 4b and 4c). [31] For the HEC phase, the dielectric relaxation peak shifted toward the low-frequency side, while a small peak appeared at  $\approx 2.5$  kHz. Although the origin of this small peak remains unclear, it has been consistently observed in the HEC phase in our previous study.[27] Notably, in the HEC region, the temperature-dependent dielectric response, in which the subpeak appears alongside the main peak according to the temperature decrease. Such a behavior differentiates the HEC phase from the conventional  $\text{N}_{\text{TBF}}$  phase.[7,13,23,29] Contrary, the  $\text{SmC}_\text{P}^\text{H}$  phase showed one relaxation peak and its peak shift accompanied by a notable reduction in its strength.

PRC measurements in the  $\text{SmA}_\text{F}$ ,  $\text{N}_{\text{TBF}}$ , HEC, and  $\text{SmC}_\text{P}^\text{H}$  phases (Figure 4d–g; Figures S11 and S12, Supporting Information) were carefully conducted upon checking the phase transitions by POM. Notably, the phase transition temperatures inevitably differed between BDS and PRC measurements because of the different cell conditions, such as thickness, used in each experiment. The temperature dependence of spontaneous polarization ( $P_\text{s}$ ) was determined using the PRC results (Figure 4h). The  $\text{N}_\text{x}$  phase exhibited  $P_\text{s} \approx 1.6 \mu\text{C cm}^{-2}$ . In the  $\text{SmA}_\text{F}$  phase,  $P_\text{s}$  depended on temperature, ranging between  $1.9$  and  $3.0 \mu\text{C cm}^{-2}$ , whereas the  $\text{N}_{\text{TBF}}$  phase exhibited an almost constant  $P_\text{s} \approx 3.0 \mu\text{C cm}^{-2}$ . Two distinct current peaks were observed in the entire HEC region—one at the crossing point of the  $E$ -field at zero and the other slightly after that. The  $E$ -field at low frequency (20 Hz) clearly split the current signal into two peaks, suggesting that the first and second peaks correspond to relaxation and spontaneous polarization reversal, respectively (Figure S13, Supporting Information). At the HEC– $\text{SmC}_\text{P}^\text{H}$  phase transition, the split peaks merged again,  $P_\text{s}$  increased continuously. Within the  $\text{SmC}_\text{P}^\text{H}$  phase,  $P_\text{s}$  gradually increased, reaching maximum values of  $4.6 \mu\text{C cm}^{-2}$ .

Finally, temperature-dependent SHG measurements were performed (Figure 4i). High SHG intensity was detected in all polar phases except the  $\text{SmC}_\text{P}^\text{H}$  region, where SHG activity was very low but not zero. In the  $\text{SmC}_\text{P}^\text{H}$  region, the sample area in the glass cell became cloudy, likely due to random alignment of the helical axis. This behavior resembles the focal conic mode of cholesteric LCs. Consequently, the incident beam was scattered, potentially preventing accurate SHG measurements. More details on SHG are provided in Section 2.5.

## 2.4. Color modulation of heliconical smectic superstructure

The  $\text{SmC}_\text{P}^\text{H}$  phase initially exhibited a strongly turbid state, yet it demonstrated the faint selective reflection color due to scattering. This turbidity may have been caused by the random orientation of the helical axes (a.k.a. focal conic state). Similarly to the already-known heliconical phases including the  $\text{N}_{\text{TBF}}$  phase, the molecules in the  $\text{SmC}_\text{P}^\text{H}$  phase were tilted at an angle  $0 < \theta < \pi/2$  with respect to the helical axis (= layer normal) (Figure 1d, e) [32]. Since in the previous heliconical phases, applying the  $E$ -field along the helical axis modulates the helical pitch ( $p$ ) and reflective color according to the continuous change in  $\theta$ , without reorienting the helical axis (**Figure 5a**). Thus, it is natural to expect the field tunable modulation of the reflected color through the pitch modulation also in the present  $\text{SmC}_\text{P}^\text{H}$  phase.

Here, an out-of-plane  $E$ -field was applied to the cell to examine the influence of the  $E$ -field on the  $\text{SmC}_\text{P}^\text{H}$  structure. The application of either DC or rectangular AC  $E$ -field perpendicular to the electrodes deformed the initial multi domains. When the  $E$ -field was applied, the helical axis gradually tilted upward along the direction of  $E$ -field, concurrently with the progressive formation of enantiomeric domains. (Figure S14, Supporting Information). And then, by gently reducing the  $E$ -field strength, large domains grew and eventually exhibited vivid red reflection at 0 V. We refer this process to as the *pretreatment process*. Although the texture still showed slight nonuniformity and light scattering even after this process, this very low birefringent state with vivid reflection was considered as a homeotropically aligned  $\text{SmC}_\text{P}^\text{H}$ , in which the helical axis, the layer normal, and the applied  $E$ -field were all parallel. In the case of the DC  $E$ -field, the reflected color changed slightly from red to orange as the  $E$ -field was increased. In contrast, applying the rectangular AC  $E$ -field allowed color modulation across the entire visible range from red to blue. This difference of the behaviors was likely attributed to the degree of charge accumulation at the electrodes, which screened the effective  $E$ -field and hindered the pitch modulation—The charges would be more accumulated in the case of the DC  $E$ -field. After pretreatment, the reflected color shifted from red to orange, yellow, green, and blue as the AC  $E$ -field was gradually increased and vice versa as the AC  $E$ -field was decreased (Figure 5c–h). When these domains were observed through a left- or right-handed circular polarizer (LCP or RCP), a clear and reversible contrast of bright and dark domains was observed, confirming the chirality in each domain (Figure 5c–h; Figure S15, Supporting Information). Interestingly, the boundary regions between the domains with opposite chirality showed almost identical reflections both for LCP and RCP, while the crossed-Nicol images exhibited extremely low transmittance (Figure S1 6, Supporting Information). This operates on the same principle of hyper-reflective cholesteric LCs [33,34], which indicates that the left- and right-

handed structures were superimposed in this region. Note that such an overlapped region was not observed in thinner cells ( $< 4.5 \mu\text{m}$ ) (Figure S17, Supporting Information).

Further, we investigated the spectroscopic properties and their response to the rectangular AC  $E$ -field (Figure 5i; Video S1, Supporting Information). First, the transmission spectrum showed only one reflection band in the visible to the near infrared spectral range (Figure S18, Supporting Information), reasonably confirming that this band corresponds to the half-pitch reflection of the heliconical structure. When the field was increased, the helical pitch decreased according to the decrease of the tilt angle, which caused blueshift of the reflection band. This electrically tunable reflection is reversible with almost no hysteresis between the forward and backward processes (Figure 5i and k; Figure S19a; Video S2, Supporting Information). More importantly, the required voltage to induce the pitch modulation was remarkably low ( $0.46\text{--}0.77 \text{ V}_{\text{pp}} \mu\text{m}^{-1}$ ). As mentioned above, the tunable range differed between the DC and rectangular AC electric-field applications, possibly due to differences in the degree of charge accumulation. Therefore, we examined the shift of the reflectance spectrum by varying the field frequency while keeping the electric-field strength. When the frequency was increased from 20 Hz to 400 Hz at  $E = 0.63 \text{ V}_{\text{pp}} \mu\text{m}^{-1}$ , the selective reflection band redshifted by approximately 150 nm. Then, the shift became saturated at higher frequencies (Figure 5j and l; Video S3, Supporting Information). Conversely, decreasing the frequency resulted in blueshift without hysteresis (Figure S19b, Supporting Information). Note that the shift showed a linear dependence on the frequency between 20 and 400 Hz in both ascending and descending processes. Thus, the color modulation can be achieved even by changing the frequency (Figure S20; Video S4, Supporting Information). In such a way, we demonstrated the straightforward modulation of the helical pitch based on both the strength and frequency of the  $E$ -field, which enabled color modulation across the visible region (Figure 5b). Although the above pitch modulation was optically stable on a timescale longer than the period of the applied AC field, certain fluctuations in color and brightness were observed in the texture under POM. The pattern of the fluctuations propagated radially, or sometimes spirally, or in more complex manners, synchronously with the applied AC  $E$ -field (Video S5 and S6, Supporting Information), so that we consider that this is attributed to the director rotation around the smectic cone. This dynamic behavior looks to be highly intriguing as a new nonequilibrium phenomenon in the polar fluid system.

## 2.5. SHG enhancement on a heliconical smectic superstructure scaffold

In the conventional nonlinear optics, the efficiency of SHG is enhanced by phase matching between the fundamental and harmonic waves.[35] In ferroelectric crystals, quasi-phase

matching is enabled by patterning an alternating polarization structure, leading to obtain efficient SHG.[35] In recent years, SHG enhancement based on the nonclassical phase matching has been successively reported in the  $N_F^*$  phase, where the phase matching condition based on photonic bandgap resonance is effectively satisfied, yielding significant SHG amplification[12,36]. Even in the  $SmC_P^H$  phase, the helicoidal polarization structure with the  $C_\infty$  symmetry may provide the similar optical condition, leading to the nonclassical phase matching to enhance the SHG efficiency (**Figure 6a**).

We propagated a polarized fundamental beam (Nd:YAG, 1064 nm) along the helical axis normal to the substrate to investigate the SHG response under the helical pitch modulation induced by  $E$ -field. As expected, the SHG signal was enhanced at  $E = 0.59 \text{ V}_{\text{pp}} \mu\text{m}^{-1}$ , and more interestingly, significantly amplified at  $E = 0.74 \text{ V}_{\text{pp}} \mu\text{m}^{-1}$  (Figure 6b). By comparing the reflectance spectra at these voltages, we found that the short-wavelength skirt of the former and the long-wavelength skirt of the latter overlap around the SHG wavelength (532 nm). This suggests that the SHG enhancement originates from phase matching coupled with the short- and long-wavelength band-edge modes at  $E = 0.74$  (band (ii) in Figure 6b) and  $0.59 \text{ V}_{\text{pp}} \mu\text{m}^{-1}$  (band (i) in Figure 6b), respectively [37]. It is well known that, for light propagation in the helical structure of the conventional  $N^*$  phase, the long- and short-wavelength band edges correspond to the extraordinary and ordinary propagation modes, respectively. In the present case, the nonlinear polarization in the  $x$ – $y$  plane is nearly parallel to the  $c$ -director and can therefore couple with the extraordinary mode, leading to a more pronounced SHG enhancement. Even then, enhancement also occurs weakly at the short-wavelength band edge, corresponding to the ordinary mode, due to the contribution from the slight off-axis component of the nonlinear polarization. Such band-edge enhancement was also predicted by optical simulation [38]. This nonclassical phase-matching behavior in the  $SmC_P^H$  phase provides distinct and tunable SHG enhancement that can be achieved using a low  $E$ -field applied along the helical axis, unlike in the  $N_F^*$  phase.[12,36] These findings offer a design guideline for tunable and efficient nonlinear optical elements.

## 2.6. Nonpolar vs polar heliconical superstructures

The final section focuses on the differences between the nonpolar and polar heliconical phases. Each phase has its unique properties, some of which look advantageous for applications. The table in Figure S21 (Supporting Information) summarizes their key properties from various point of views. Importantly, the  $SmC_P^H$  phase provides certain benefits over the nonpolar heliconical nematic phase: (1) it forms a polar heliconical structure despite being a single-component system, whereas the nonpolar heliconical nematic phase is a complex system of an

LC mixture doped with a chiral molecule; (2) although two chiral domains exist, uniformly homeotropically aligned domains can be obtained without an alignment layer, whereas the nonpolar heliconical nematic phase requires an alignment layer to achieve uniform homeotropic alignment [13,7,32]; (3) the driving voltage required for color modulation across the entire visible wavelength range is much lower (approximately one-third of that for heliconical nematics) [39]; (4) although both phases can realize frequency-driven color modulation, the  $\text{SmC}_\text{P}^\text{H}$  phase operates at much lower frequencies (10 Hz to sub-kHz) than heliconical nematics (several kHz to sub-MHz), which is highly advantageous for suppressing dielectric heating [40]; (5) since the polar system allows access to even-order nonlinear optical processes, the helielectric structure enables unique SHG enhancement through the special phase matching, as demonstrated above. Taking these advantages, the  $\text{SmC}_\text{P}^\text{H}$  phase offers a simple system with high optical quality and throughput through the straightforward orientation of the helical axis, making it promising for optical applications, such as cavity-less lasing and up-conversion devices based on cavity-less lasing.[41]

### 3. Conclusion

In this study, we performed a detailed analysis of the  $\text{SmA}_\text{F}$ – $\text{N}_{\text{TFB}}$ –HEC– $\text{SmC}_\text{P}^\text{H}$  phase transitions in a novel polar molecule (Compound **1**), involving hierarchical symmetry breaking. Introducing a single fluorine atom into the previous molecule (Model I), which exhibited the  $\text{N}_\text{F}$ –HEC phase transition sequence, made the phase transition behavior more complicated. The emergence of such diverse polar phases is highly sensitive to the molecular structure, even to minute structural variations in the terminal alkyl ester groups. This will likely be interpreted by rational molecular design directed by advanced theoretical framework in the future [42–44].

During the phase transition from the HEC to the  $\text{SmC}_\text{P}^\text{H}$  phase, a distinct first-order phase transition was observed, accompanied by characteristic changes in POM textures, as well as the discontinuous behaviors in BDS, PRC, and SHG, all of which clearly demonstrate the structural transition. Furthermore, the  $\text{SmC}_\text{P}^\text{H}$  phase demonstrates ultralow-voltage color modulation and remarkable SHG amplification based on nonclassical phase matching. These results not only deepen our understanding of the hierarchical construction of polar order but also provide important insights that broaden the potential applications of polar fluid materials. We believe that our present study may offer new guidelines for the design of advanced polar fluids and contribute to the development of state-of-the-art functional materials.

### Data availability

The authors declare that the data supporting the findings of this study are available within the paper and its supporting information files. All other information is available from the corresponding authors upon reasonable request.

### **Acknowledgements**

We are grateful to Dr. H. Koshino (RIKEN, CSRS) for allowing us to use JNM-ECZ500 (500 MHz, JEOL). We wish to thank Dr. Nogawa (RIKEN, CSRS) for the HRESI-MS measurement. We would like to acknowledge the Hokusai GreatWave Supercomputing Facility (project no. RB230008) at the RIKEN Advanced Center for assistance in computing and communication. This work was partially supported by JSPS KAKENHI (JP22K14594; H.N., 23K26573; H.Y., JP21H01801, JP23K17341; F.A.), RIKEN Incentive Research Projects (FY2024: H.N.), JST CREST (JPMJCR23O1; K.S., F.A.) and JST SICORP EIG CONCERT-Japan (JPMJSC22C3; F.A.).

### **Contributions**

H.N. and F.A. conceived the project and designed the experiments. H.N. designed molecules and performed DFT calculation. A.N. synthesized and characterized all compound. H.N. carried out DSC, POM, BDS, PRC and UV-vis-NIR spectra studies. H.Y. constructed reflection spectra measurement system and recorded spectra. D.K. performed SHG measurements. K.S. and H.N. took XRD measurements. H.N. and F.A. analyzed data and discussed the results. H.N. and F.A. wrote the manuscript, and all authors approved the final manuscript.

### **Corresponding authors**

Correspondence to Hiroya Nishikawa or Fumito Araoka

### **Competing interests**

The authors declare no competing interests.

Received: ((will be filled in by the editorial staff))

Revised: ((will be filled in by the editorial staff))

Published online: ((will be filled in by the editorial staff))

## References

1. R. J. Mandle, S. J. Cowling, J. W. Goodby, *Phys. Chem. Chem. Phys.* **2017**, *19*, 11429.
2. H. Nishikawa, K. Shiroshita, H. Higuchi, Y. Okumura, Y. Haseba, S. Yamamoto, K. Sago, H. Kikuchi, *Adv. Mater.* **2017**, *29*, 1702354.
3. X. Chen, E. Korblova, D. Dong, X. Wei, R. Shao, L. Radzihovsky, M. A. Glaser, J. E. Maclennan, D. Bedrov, D. M. Walba, N. A. Clark, *Proc. Natl. Acad. Sci. U.S.A.* **2020**, *117*, 14021.
4. N. Sebastián, M. Čopič, A. Mertelj, *Phys. Rev. E*, **2022**, *106*, 021001.
5. Q. Liao, S. Aya, M. Huang, *Liq. Cryst. Rev.* **2024**, *12*, 149.
6. X. Chen, V. Martinez, P. Nacke, E. Korblova, A. Manabe, M. K.-Memmer, G. Freychet, M. Zhernenkov, M. A. Glaser, L. Radzihovsky, J. E. Maclennan, D. M. Walba, M. Bremer, F. Giesselmann, N. A. Clark, *Proc. Natl. Acad. Sci. U.S.A.* **2022**, *22*, e2210062119.
7. H. Nishikawa, D. Okada, D. Kwaria, A. Nihonyanagi, M. Kuwayama, M. Hoshino, F. Araoka, *Adv. Sci.* **2024**, *11*, 2405718.
8. G. J. Strachan, E. Górecka, J. Szydłowska, A. Makal, D. Pociecha, *Adv. Sci.* **2025**, *12*, 2409754.
9. G. Strachan, S. Ramsay, M. Juodka, D. Pociecha, J. Szydłowska, J. M. D. Storey, N. Vaupotic, R. Walker, E. Górecka, *Angew. Chem. Int. Ed.*, **2025**, e202516302.
10. H. Nishikawa, F. Araoka, *Adv. Mater.* **2021**, *33*, 2101305.
11. C. Feng, R. Saha, E. Korblova, D. Walba., S. N. Sprunt, A. Jakli, *Adv. Opt. Mater.* **2021**, *9*, 2101230.
12. X. Zhao, J. Zhou, J. Li, J. Kougo, Z. Wan, M. Huang, Satoshi Aya, *PNAS*, **2021**, *118*, e2111101118.
13. J. Karcz, J. Herman, N. Rychłowicz, P. Kula, E. Górecka, J. Szydłowska, P. W. Majewski, D. Pociecha, *Science* **2024**, *384*, 1096.
14. J. Hobbs, C. J. Gibb, R. J. Mandle, *Nat. Commun.* **2025**, *16*, 7510.
15. H. Kikuchi, H. Nishikawa, H. Matsukizono, S. Iino, T. Sugiyama, T. Ishioka, Y. Okumura, *Adv. Sci.* **2024**, *11*, 2409827.
16. J. Hobbs, C. J. Gibb, D. Pociecha, J. Szydłowska, E. Górecka, R. J. Mandle, *Angew. Chem. Int. Ed.* **2024**, e202416545.

17. Y. Song, M. Deng, Z. Wang, J. Li, H. Lei, Z. Wan, R. Xia, S. Aya, M. Huang, *J. Phys. Chem. Lett.* **2022**, *13*, 9983.

18. H. Nishikawa, M. Kuwayama, A. Nihonyanagi, B. Dhara, F. Araoka, *J. Mater. Chem. C*, **2023**, *11*, 12525.

19. P. Pieranski, *Chirality in Liquid Crystals* (Eds: H.-S. Kitzerow, C. Bahr), Springer-Verlag, New York 2001, Ch. 2.

20. X. Zhao, J. Zhou, J. Li, J. Kougo, Z. Wan, M. Huang, Satoshi Aya, *PNAS*, **2021**, *118*, e2111101118.

21. D. Pociecha, R. Walker, E. Cruickshank, J. Szydłowska, P. Rybak, A. Makal, J. Matraszek, J. M. Wolska, J. M. D. Storey, C. T. Imrie, E. Górecka, *J. Mol. Liq.* **2022**, *361*, 119532.

22. C. J. Gibb, J. Hobbs, D. I. Nikolova, T. Raistrick, S. R. Berrow, A. Mertelj, N. Osterman, N. Sebastián, H. F. Gleeson, Richard. J. Mandle, *Nat Commun* **2024**, *15*, 5845.

23. E. Górecka, M. Majewska, L. Fekete, J. Karcz, J. Żukowska, J. Herman, P. Kula, D. Pociecha, *Mater. Horiz.* **2025**, *12*, 5352.

24. H. Wang, I. Bala, R. A. Wiscons, I. Aprahamian, *Adv. Mater.* **2025**, e09125.

25. C. L. Folcia, J. Ortega, T. Sierra, A. Martínez-Bueno, J. Etxebarria, *Giant*, **2024**, *19*, 100316.

26. A. B. Szukalska, J. Karcz, J. Herman, D. Pociecha, E. Górecka, P. Kula, J. Myśliwiec, *Adv. Mater.* **2025**, e11648.

27. H. Nishikawa, D. Kwaria, A. Nihonyanagi, F. Araoka, *Adv. Mater.* **2025**, e13451, <http://doi.org/10.1002/adma.202513451>.

28. J. Hobbs, C. J. Gibb, R. J. Mandle, *Small Sci.* **2024**, *4*, 2400189.

29. G. J. Strachan, E. Górecka, D. Pociecha, *Mater. Horiz.*, **2025**, <https://doi.org/10.1039/D5MH01674F>.

30. A. Erkoreka, A. Mertelj, M. Huang, S. Aya, N. Sebastián, J. M.-Perdiguero, *J. Chem. Phys.* **2023**, *159*, 184502.

31. D. Węglowska, M. Czerwiński, R. Dzienisiewicz, P. Perkowski, J. Szydłowska, D. Pociecha, M. Mrukiewicz, *J. Mater. Chem. C*, **2025**, *13*, 9545.

32. J. Xiang, Y. Li, Q. Li, D. A. Paterson, J. M. D. Storey, C. T. Imrie, O. D. Lavrentovich, *Adv. Mater.* **2015**, *27*, 3014.

33. D. M. Makow, *Appl. Opt.* **1980**, *19*, 1274.

34. M. E. McConney, V. P. Tondiglia, J. M. Hurtubise, L. V. Natarajan, T. J. White, T. J. Bunning, *Adv. Mater.*, **2011**, *23*, 1453.

35. R. W. Boyd, “Chapter 2, page 69–133-Wave-Equation Description of Nonlinear Optical Interactions.” in *Nonlinear Optics*. 3rd ed., Academic Press 2008.

36. X. Zhao, H. Long, H. Xu, J. Kougo, R. Xia, J. Li, M. Huang, Satoshi Aya, *PNAS*, **2022**, *119*, e2205636119.

37. P. G. de Gennes, J. Prost, *The Physics of Liquid Crystals*, 2nd ed., Oxford University, Oxford 1995.

38. J. Ortega, C.L. Folcia, J. Etxebarria, *Opt. Express*, **2023**, *31*, 36966.

39. C. Yuan, H. Liu, Y. Zhan, X. Liu, Y. Tang, H. Hu, Z.-G. Zheng, Q. Li, *Adv. Mater.* **2025**, *37*, 2507000.

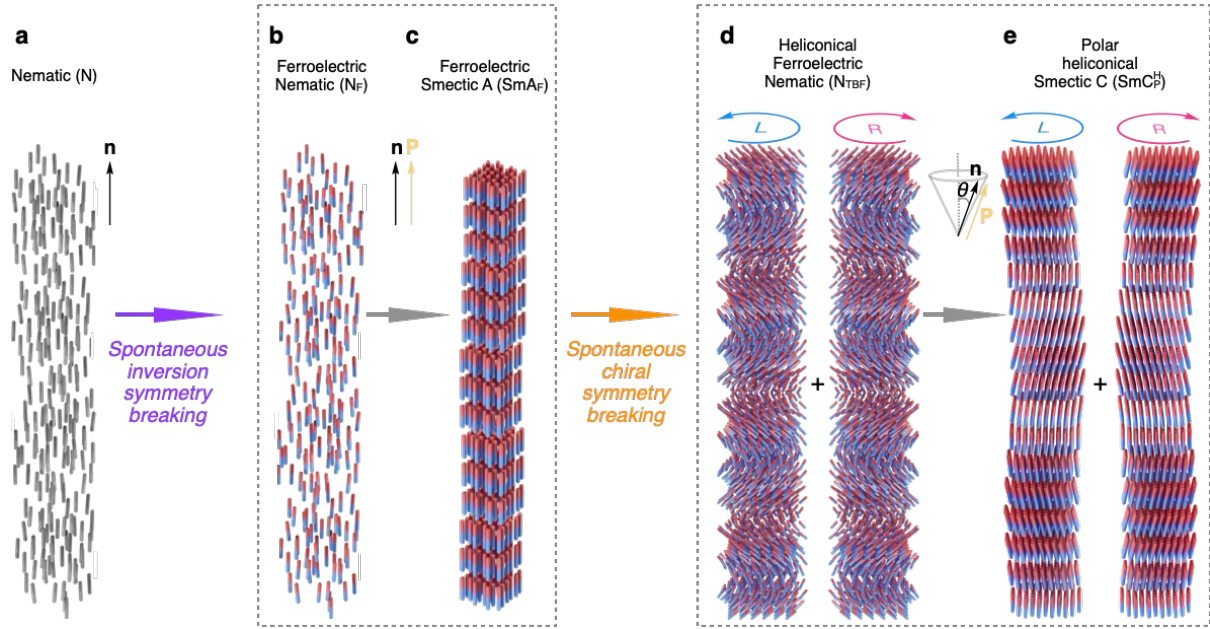
40. B. Liu, C.-L. Yuan, H.-L. Hu, H. Wang, Y.-W. Zhu, P.-Z. Sun, Z.-Y. Li, Z.-G. Zheng, Quan Li, *Nat. Commun.* **2022**, *13*, 2712.

41. D. Okada, H. Nishikawa, F. Araoka, *Adv. Sci.* **2024**, 2405227.

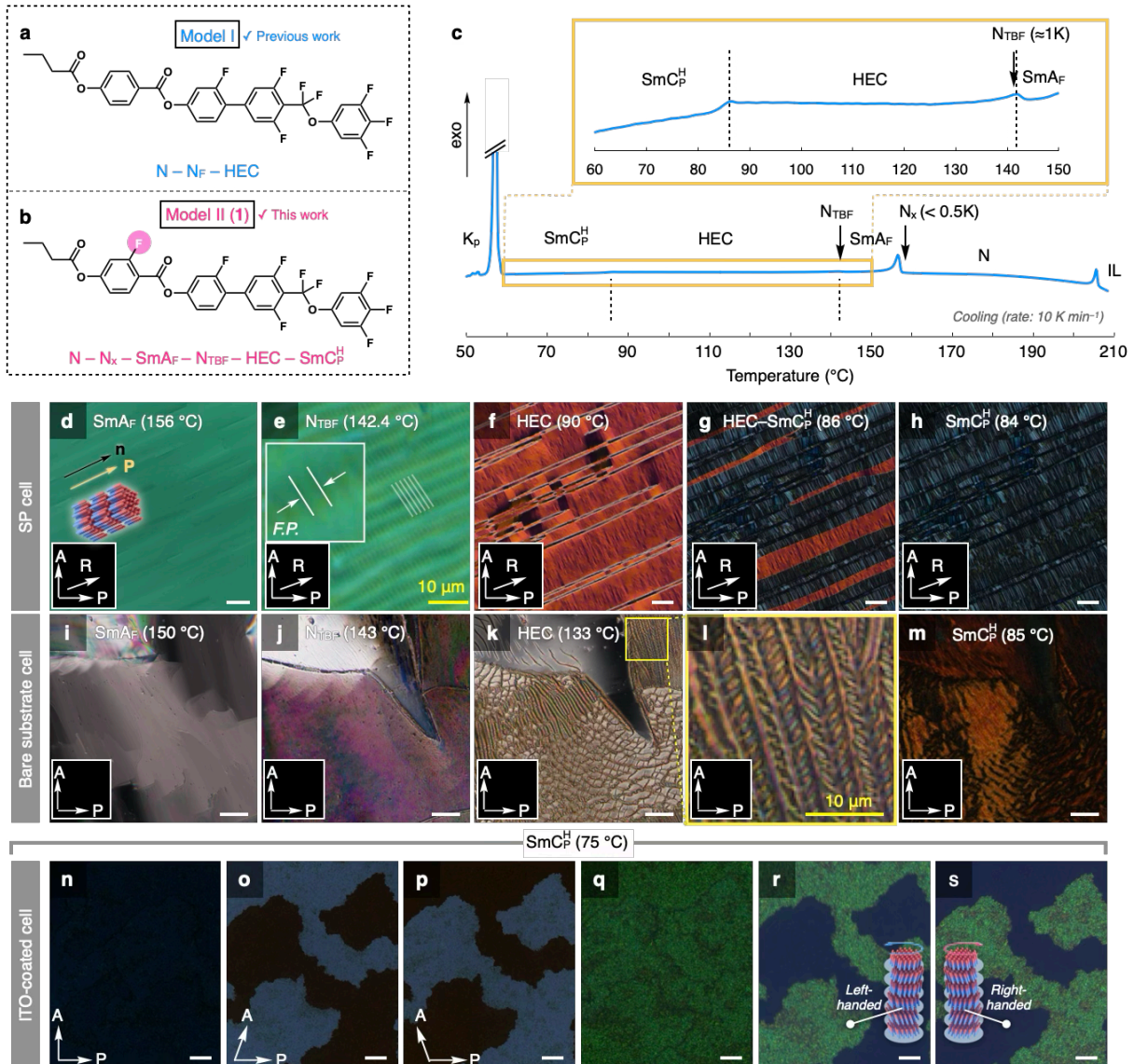
42. G. J. Gibb, J. Hobbs, R. J. Mandle, *J. Am. Chem. Soc.* **2025**, *147*, 4571.

43. G. J. Strachan, E. Górecka, J. Hobbs, D. Pociecha, *J. Am. Chem. Soc.*, **2025**, *147*, 6058.

44. M. Czerwiński, M. Mrukiewicz, M. Filipow, D. Pociecha, N. Podoliak, D. Repček, M. Zajac, D. Węglowska, *Chem. Mater.* **2025**, *19*, 8077.



**Figure 1** Schematic of the phase transition sequence for a polar material via hierarchical symmetry breaking (**n**: director and **P**: polarization vector). All phases except for the nematic (N) phase lack a head–tail orientation equivalence, so polar order occurs (i.e.,  $\mathbf{n} \neq -\mathbf{n}$ ). The  $\text{N}_F$  phase emerge via spontaneous inversion symmetry breaking from the isotropic or N phase. The same pathway offers a transition to the  $\text{SmA}_F$  phase with additional layer positional ordering. Subsequent spontaneous chiral symmetry breaking generates unique helielectric phases (i.e.,  $\text{N}_{\text{TBF}}$  and  $\text{SmC}_P^H$ ) in which **n** and **P** are tilted at an angle  $0 < \theta < \pi/2$  with respect to the helical axis. In both phases, left (*L*)- and right (*R*)-handed helices are formed with equal probability.



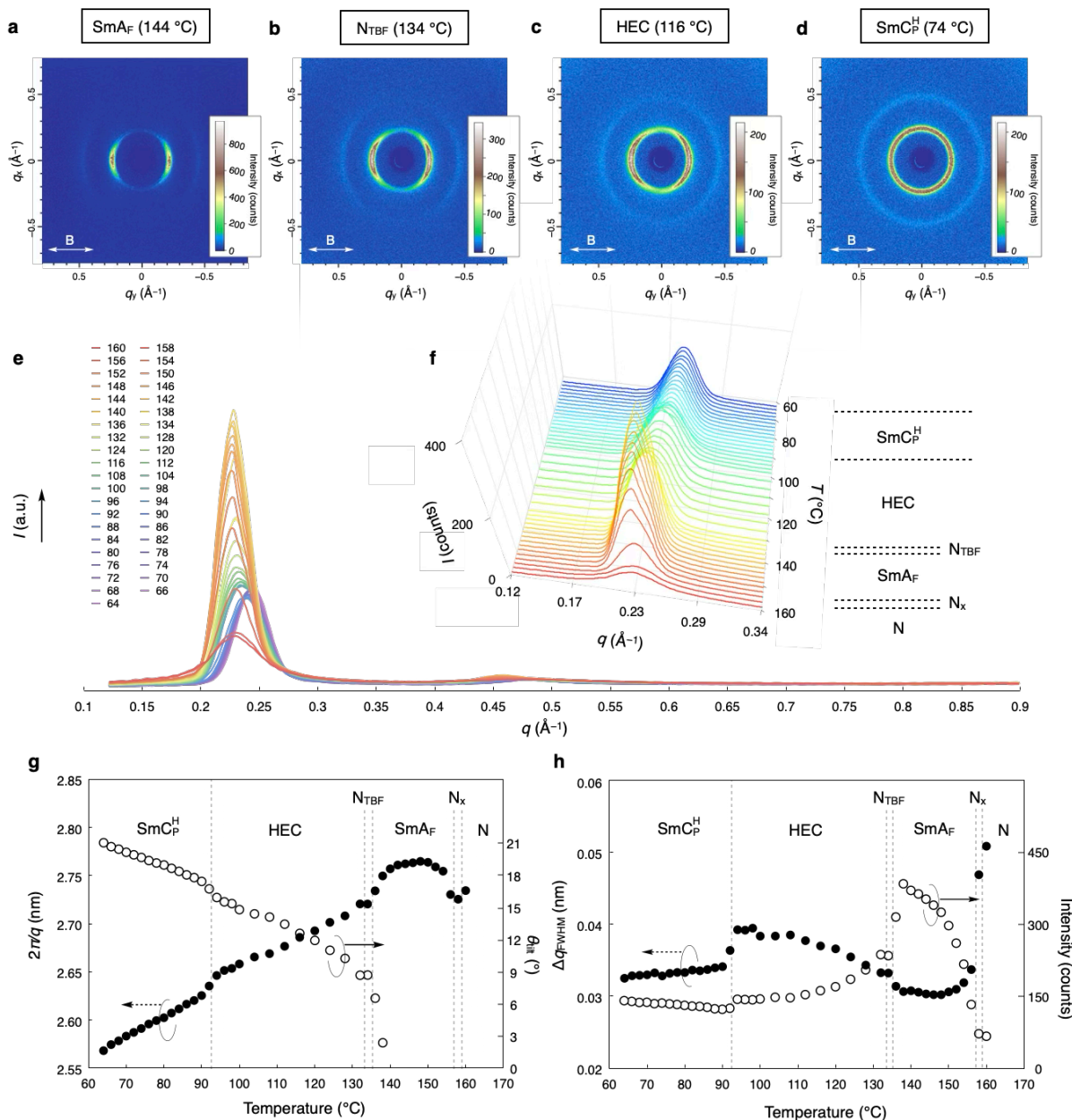


**Figure 3** XRD profiles for Compound 1. 2D WAXS patterns obtained under a magnetic field ( $\sim 1 \text{ T}$ ,  $\mathbf{B} \parallel \mathbf{n}$ ) of the (a)  $\text{SmA}_F$ , (b)  $\text{N}_{\text{TFB}}$ , (c) HEC, and (d)  $\text{SmCP}^H$  phases. (e) 1D and (f) 3D X-ray diffractograms generated by box-scan analysis of the 2D WAXS profile. (g)  $2\pi/q$  and tilt angle ( $\theta_{\text{tilt}}$ ) vs temperature. (h)  $\Delta q_{\text{FWHM}}$  and intensity vs temperature.

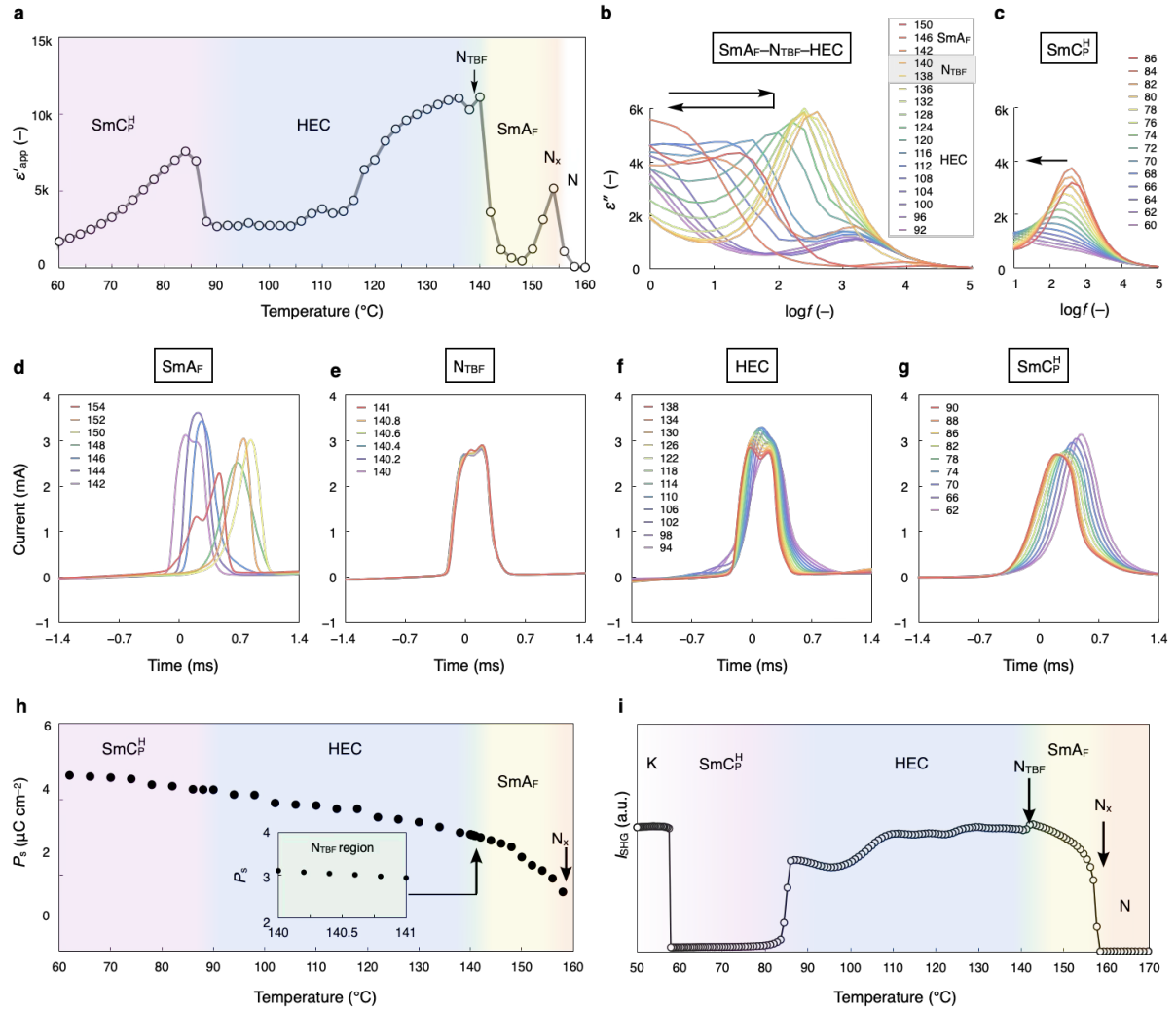


**Figure 4** Polar behavior of Compound 1. (a) Apparent dielectric permittivity ( $\epsilon'_{app}$ ) vs temperature. Dielectric loss ( $\epsilon''$ ) vs frequency for the (b)  $\text{SmA}_F\text{--HEC}$  phase transition and (c) in the  $\text{SmC}_P^H$  phase. Black arrows indicate direction of peak shift. PRC profiles of the (d)  $\text{SmA}_F$ , (e)  $\text{N}_\text{TBF}$ , (f) HEC, and (g)  $\text{SmC}_P^H$  phases. Temperature-dependent (h) spontaneous polarization  $P_s$ , and (i) SHG.

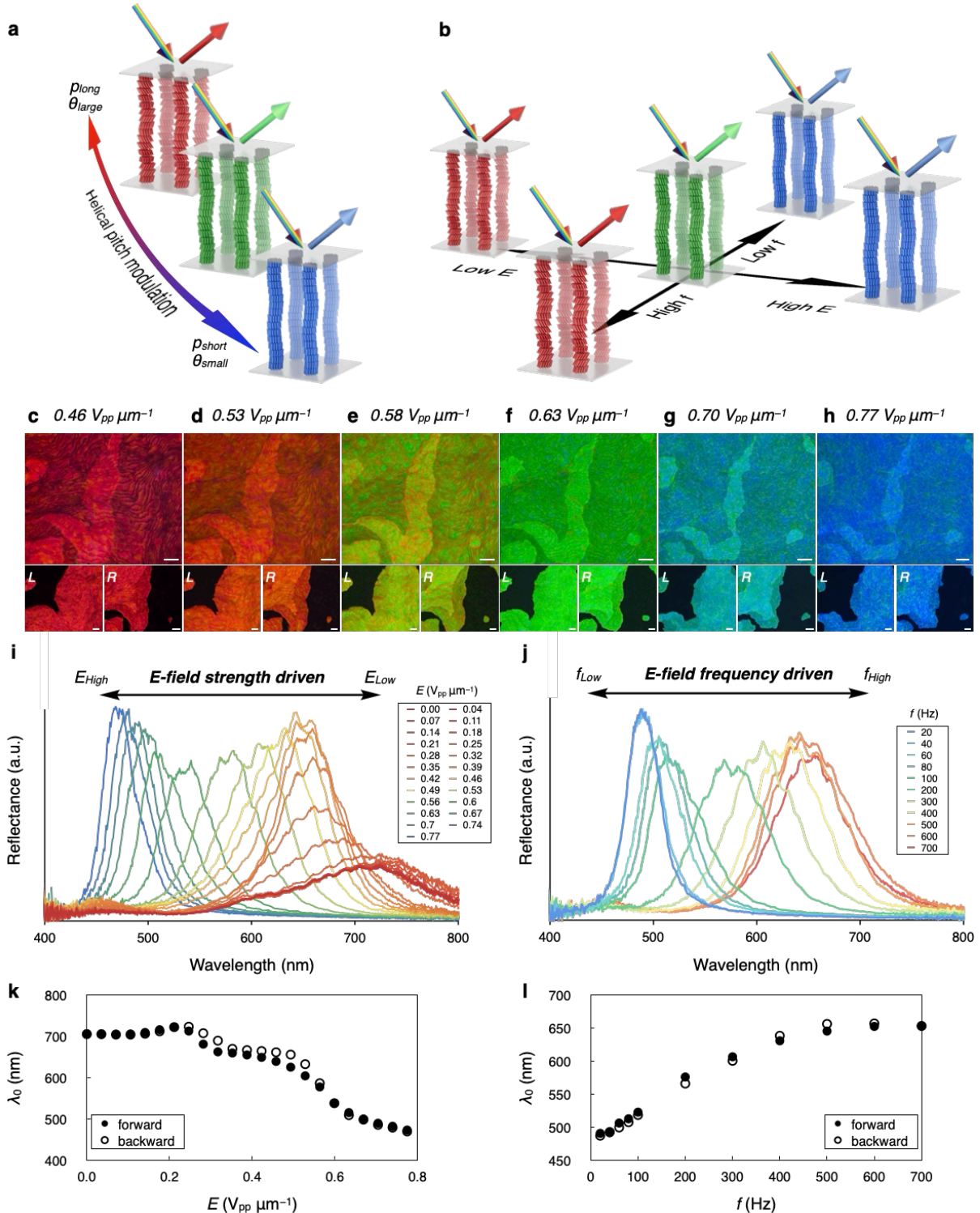


**Figure 5** Color modulation in the  $\text{SmC}_\text{P}^{\text{H}}$  phase of Compound **1** ( $T = 75^\circ\text{C}$ ). Schematic illustrations of (a) modulation of the reflected color associated with the helical pitch and (b) color modulation driven by the  $E$ -field strength and frequency. (c–h) Evolution of reflected color in reflection-mode POM (RPOM) images taken after pretreatment process. The bottom images were taken with left- and right-circular polarizers (symbol: L and R). Scale bar: 200  $\mu\text{m}$ . Evolution of reflection spectra by modulation of the (i)  $E$ -field strength and (j) frequency. Central wavelength ( $\lambda_0$ ) vs (k)  $E$ -field strength and (l)  $E$ -field frequency.

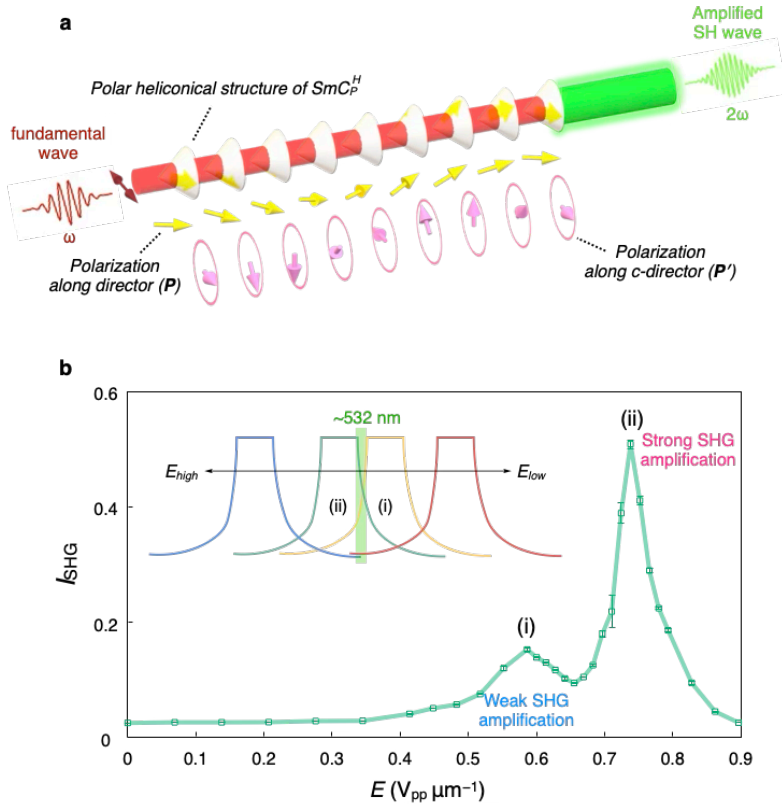


**Figure 6** SHG amplification in the  $\text{SmC}_\text{P}^{\text{H}}$  phase: (a) schematic illustration and (b) SHG intensity vs  $E$ -field. The upper inset shows the ideal reflection band modulated by the  $E$ -field. The wavelength of the emitted SH light at  $\approx 532$  nm matches the band edge on the (i) short-wavelength or (ii) long-wavelength side.

## Supplementary Information

### *Electrically Tunable Heliconical Smectic Superstructure in Polar Fluids*

Hiroya Nishikawa\*, Dennis Kwaria, Atsuko Nihonyanagi, Koki Sano, Hiroyuki Yoshida and  
Fumito Araoka\*

\*To whom correspondence should be addressed.

E-mail: [hiroya.nishikawa@riken.jp](mailto:hiroya.nishikawa@riken.jp) (H.N.), [fumito.araoaka@riken.jp](mailto:fumito.araoaka@riken.jp) (F.A.)

#### Table of contents

##### Methods

1. General and materials .....
2. Synthesis and characterization .....

Supplementary Figures (Figures S1–S26) .....
--

Supplementary Tables (Tables S1, S2) .....
--

Supplementary Video (Video S1–S6) .....
---

Supplementary References .....
--------------------------------

## Methods

### 1. General and materials

**Nuclear magnetic resonance (NMR) spectroscopy:**  $^1\text{H}$ ,  $^{13}\text{C}$ , and  $^{19}\text{F}$  NMR spectra were recorded on JNM-ECZ500 (JEOL) operating at 500 MHz, 126 MHz, and 471 MHz for  $^1\text{H}$  [ $^1\text{H}\{^{19}\text{F}\}$ ],  $^{13}\text{C}\{^1\text{H}\}$  [ $^{13}\text{C}\{^1\text{H},^{19}\text{F}\}$ ] and  $^{19}\text{F}$  [ $^{19}\text{F}\{^1\text{H}\}$ ] NMR, respectively, using the TMS (trimethylsilane) as an internal standard for  $^1\text{H}$  NMR and the deuterated solvent for  $^{13}\text{C}$  NMR. The absolute values of the coupling constants are given in Hz, regardless of their signs. Signal multiplicities were abbreviated by s (singlet), d (doublet), t (triplet), q (quartet), quint (quintet), sext (sextet), and dd (double–doublet), respectively.

**High-resolution mass (HRMS) spectroscopy:** The high-resolution electrospray ionization mass spectrometry (HRESI-MS) was performed on SYNAPT G2-S/UPLC system (Waters ltd.).

**Density Functional Theory (DFT) Calculation:** Calculations were performed using the Chem3D (pro, 22.2.0.3300) and Gaussian 16 (G16, C.01) softwares (installed at the RIKEN Hokusai GreatWave Supercomputing facility) for MM2 and DFT calculations, respectively. GaussView 6 (6.0.16) software was used to visually analyze the calculation results. [S1] Dipole moments of molecules were calculated using b3lyp-gd3bj/6-311+g(d,p) level. The calculation method is as follows: opt=tight b3lyp-gd3bj/6-311+g(d,p) geom=connectivity empiricaldispersion=gd3bj int=ultrafine.

**Polarized optical microscopy (POM):** Polarized optical microscopy was performed on a polarizing microscope (Eclipse LV100 POL, Nikon) with a hot stage (HSC402, INSTECH) on the rotation stage. Unless otherwise noted, the sample temperature was controlled using the INSTECH temperature controller (mk2000, INSTECH).

**Differential scanning calorimetry (DSC).** Differential scanning calorimetry was performed on a calorimeter (DSC3+, Mettler-Toledo). Rate: 10 K min<sup>-1</sup>. Cooling/heating profiles were recorded and analyzed using the Mettler-Toledo STARe software system.

**Dielectric spectroscopy.** Dielectric relaxation spectroscopy was performed ranging between 1 Hz and 1 MHz using an impedance/gain-phase analyzer (SI 1260, Solartron Metrology) and a dielectric interface (SI 1296, Solartron Metrology). Prior to starting the measurement of the LC sample, the capacitance of the empty cell was determined as a reference. The temperature was controlled using a homemade heater block and temperature controller. The automatic measurement was taken place by the LabVIEW software programming.

**PRC measurement.** PRC measurements were performed in the temperature range of the polar phase under a triangular-wave  $E$ -field using a ferroelectricity evaluation system (FCE 10, TOYO Corporation), which is composed of an arbitrary waveform generator (2411B), an IV/QV amplifier (model 6252) and a simultaneous A/D USB device (DT9832).

**SHG/SHM measurements.** The SHG/SHM investigation was carried out using a Q-switched DPSS Nd: YAG laser (FQS-400-1-Y-1064, Elforlight) at  $\lambda = 1064$  nm with a 5 ns pulse width (pulse energy: 400  $\mu$ J). The primary beam was incident on the LC cell followed by the detection of the SHG signal. The electric field was applied normally to the LC cell.

**Wide-angle X-ray diffraction (WAXD) analysis.** 2D WAXD measurement was performed using NANOPIX system (Rigaku). The samples held in a homemade holder with magnets (Figure S22) was measured at a constant temperature using a temperature controller and a hot stage (mk2000, INSTECH) with high temperature-resistance samarium cobalt magnets ( $\sim 1$  T, Shimonishi Seisakusho Co., Ltd.). The scattering vector  $q$  ( $q = 4\pi\sin\theta/\lambda$ ;  $2\theta$  and  $\lambda$  = scattering angle and wavelength of an incident X-ray beam (1.54 Å) and position of an incident X-ray beam on the detector were calibrated using several orders of layer diffractions from silver behenate ( $d = 58.380$  Å). The sample-to-detector distances were 82.20 mm, where acquired scattering 2D images were integrated along the Debye–Scherrer ring by using software (Igor Pro with Nika-plugin), affording the corresponding one-dimensional X-ray diffraction profiles.

#### Information of used liquid crystalline (LC) cells:

##### ITO glass cell (EHC):

- ITO-coated type, electrode area:  $5 \times 10$  mm
- Experiments: POM (thickness: 10.0 and 25.0  $\mu$ m) and DR (thickness: 10.0  $\mu$ m)

##### ITO glass cell (homemade):

- (case i) ITO-coated type (non-alignment layer), electrode area:  $4 \times 5$  mm
- (case i) Experiments: PRC (thickness: 4.6  $\mu$ m) studies
- (case ii) ITO-coated type (silanized layer), electrode area:  $4 \times 5$  mm
- (case ii) Experiments: Pitch modulation (thickness: 14.1  $\mu$ m) studies

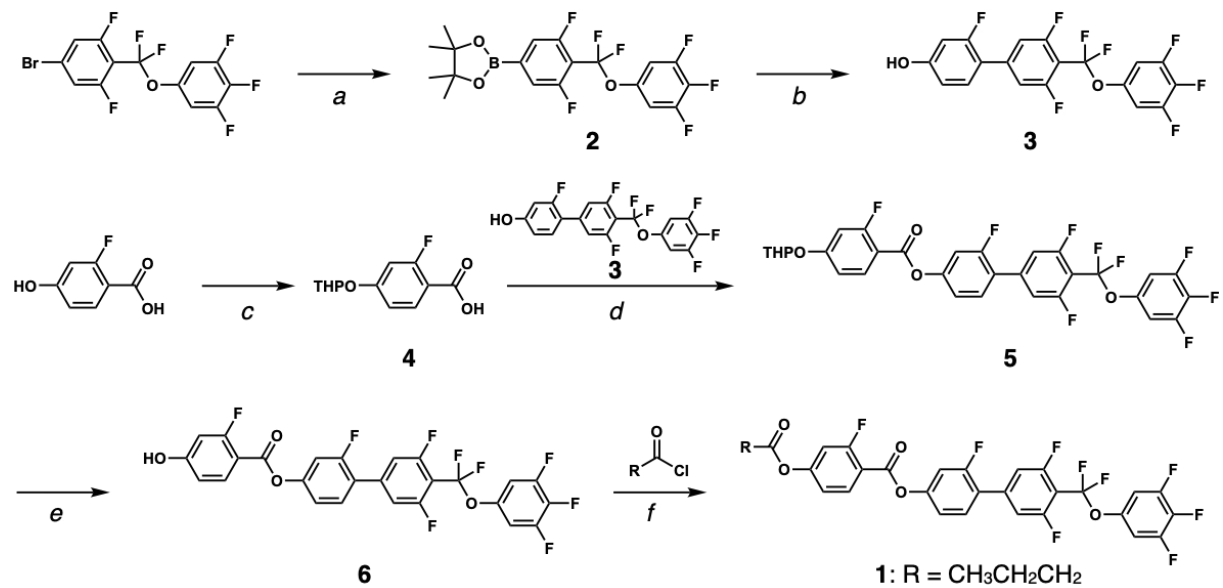
##### Synparallel-rubbed (SP) cell (EHC):

- PI-coated type, thickness: 5.0  $\mu$ m
- Alignment layer: LX-1400
- Experiments: POM studies

## 2. Synthesis of Compound 1.

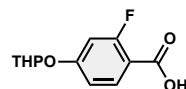
### 2.1. Synthetic route

All compounds (**1–6**) were synthesized according to previous literature [S2] (Scheme S1). NMR and MS spectra for final target **1** are shown in Figure S23–S26.



**Scheme S1** Synthetic pathway of Compound **1**. a)  $\text{B}_2\text{pin}_2$ ,  $\text{Pd}(\text{dppf})\text{Cl}_2\text{-CH}_2\text{Cl}_2$ ,  $\text{KOAc}$ , 1,4-dioxane, MM400 (30 Hz), 110 °C, 10 min, b)  $\text{Pd}(\text{OAc})_2$ , SPhos,  $\text{K}_2\text{CO}_3$ , THF/H<sub>2</sub>O, 55 °C, 3 h, c) 3,4-dihydro-2H-pyran,  $\text{Et}_2\text{O}$ , 35 °C, 2.5 h; r.t., 20 h, d) **3**, EDAC-HCl, DMAP,  $\text{CH}_2\text{Cl}_2$ , 0 °C, 1 h; r.t., 1 h, e) *p*-TsOH,  $\text{CH}_2\text{Cl}_2\text{/MeOH}$ , 50 °C, 1.5 h, f) TEA,  $\text{CH}_2\text{Cl}_2$ , 0 °C; r.t.

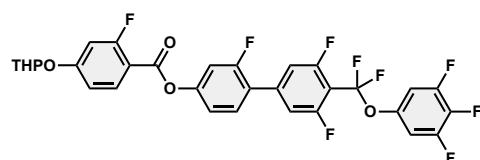
### 2.2.1. Synthesis of 2-fluoro-4-((tetrahydro-2H-pyran-2-yl)oxy)benzoic acid (4)



$^1\text{H}\{^{19}\text{F}\}$ -NMR (500 MHz,  $\text{CDCl}_3$ ):  $\delta$  7.97 (d,  $J = 8.7$  Hz, 1H), 6.90–6.86 (m, 2H), 5.50 (t,  $J = 2.7$  Hz, 1H), 3.85–3.80 (m, 1H), 3.65 (dt,  $J = 11.3, 3.9$  Hz, 1H), 2.04–1.95 (m, 1H), 1.90–1.87 (m, 2H), 1.77–1.67 (m, 2H), 1.63–1.60 (m, 1H)

$^{19}\text{F}\{^1\text{H}\}$ -NMR (471 MHz,  $\text{CDCl}_3$ ):  $\delta$  –105.0

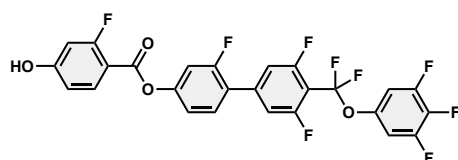
### 2.2.2. Synthesis of 4'-(difluoro(3,4,5-trifluorophenoxy)methyl)-2,3',5'-trifluoro-[1,1'-biphenyl]-4-yl 2-fluoro-4-((tetrahydro-2H-pyran-2-yl)oxy)benzoate (5)



$^1\text{H}\{^{19}\text{F}\}$ -NMR (500 MHz,  $\text{CDCl}_3$ ):  $\delta$  8.04 (d,  $J = 8.7$  Hz, 1H), 7.48 (d,  $J = 8.0$  Hz, 1H), 7.22 (s, 2H), 7.18–7.16 (m, 2H), 7.00 (d,  $J = 5.6$  Hz, 2H), 6.96–6.91 (m, 2H), 5.53 (t,  $J = 3.0$  Hz, 1H), 3.86–3.81 (m, 1H), 3.68–3.64 (m, 1H), 2.04–1.96 (m, 1H), 1.92–1.90 (m, 2H), 1.76–1.68 (m, 2H), 1.65–1.61 (m, 1H)

$^{19}\text{F}\{^1\text{H}\}$ -NMR (471 MHz,  $\text{CDCl}_3$ ):  $\delta$  –61.7 (t,  $J = 27.3$  Hz, 2F), –104.1 (s, 1F), –110.4 (t,  $J = 27.6$  Hz, 2F), –113.9 (s, 1F), –132.3 (d,  $J = 18.4$  Hz, 2F), –163.0 (t,  $J = 21.9$  Hz, 1F)

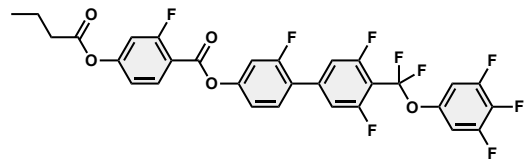
### 2.2.3. Synthesis of 4'-(difluoro(3,4,5-trifluorophenoxy)methyl)-2,3',5'-trifluoro-[1,1'-biphenyl]-4-yl 2-fluoro-4-hydroxybenzoate (6)



$^1\text{H}\{^{19}\text{F}\}$ -NMR (500 MHz,  $\text{CDCl}_3$ ):  $\delta$  8.03 (d,  $J = 8.7$  Hz, 1H), 7.48 (d,  $J = 8.6$  Hz, 1H), 7.22 (s, 2H), 7.18–7.16 (m, 2H), 7.00 (d,  $J = 5.7$  Hz, 2H), 6.75 (dd,  $J = 8.6, 2.4$  Hz, 1H), 6.70 (d,  $J = 2.4$  Hz, 1H), 5.76 (s, 1H)

$^{19}\text{F}\{^1\text{H}\}$ -NMR (471 MHz,  $\text{CDCl}_3$ ):  $\delta$  –61.7 (t,  $J = 25.7$  Hz, 2F), –104.0 (s, 1F), –110.3 (t,  $J = 25.9$  Hz, 2F), –113.9 (s, 1F), –132.3 (d,  $J = 22.1$  Hz, 2F), –163.0 (t,  $J = 22.1$  Hz, 1F)

### 2.2.4. Synthesis of 4'-(difluoro(3,4,5-trifluorophenoxy)methyl)-2,3',5'-trifluoro-[1,1'-biphenyl]-4-yl 4-(butyryloxy)-2-fluorobenzoate (Compound 1)



White powder, 84.9% yield

$^1\text{H}\{^{19}\text{F}\}$ -NMR (500 MHz,  $\text{CDCl}_3$ ):  $\delta$  8.14 (dd,  $J = 7.8, 1.5$  Hz, 1H), 7.50 (dd,  $J = 7.9, 0.9$  Hz, 1H), 7.23 (s, 2H), 7.20–7.18 (m, 2H), 7.10–7.08 (m, 2H), 7.00 (d,  $J = 5.6$  Hz, 2H), 2.59 (t,  $J = 7.4$  Hz, 2H), 1.81 (td,  $J = 14.8, 7.4$  Hz, 2H), 1.07 (t,  $J = 7.4$  Hz, 3H)

$^{19}\text{F}\{^1\text{H}\}$ -NMR (471 MHz,  $\text{CDCl}_3$ ):  $\delta$  -61.7 (t,  $J = 25.7$  Hz, 2F), -103.9 (s, 1F), -110.3 (t,  $J = 25.7$  Hz, 2F), -113.6 (s, 1F), -132.3 (d,  $J = 18.4$  Hz, 2F), -163.0 (t,  $J = 21.9$  Hz, 1F)

$^{13}\text{C}\{^1\text{H},^{19}\text{F}\}$ -NMR (126 MHz,  $\text{CDCl}_3$ ):  $\delta$  171.0, 162.8, 161.5, 159.9, 159.5, 156.1, 151.9, 151.0, 144.6, 140.7, 138.5, 133.4, 130.6, 123.4, 120.1 (t,  $J = 262.5$  Hz), 118.4, 117.8, 114.6, 113.1, 111.2, 110.9, 108.9 (t,  $J = 32.1$  Hz), 107.5, 36.1, 18.2, 13.6

ESI-HRMS (m/z):  $[\text{M}+\text{Na}^+]$  calc for 651.0830; found, 651.0834

## Supplementary Figures (Figures S1–S26)

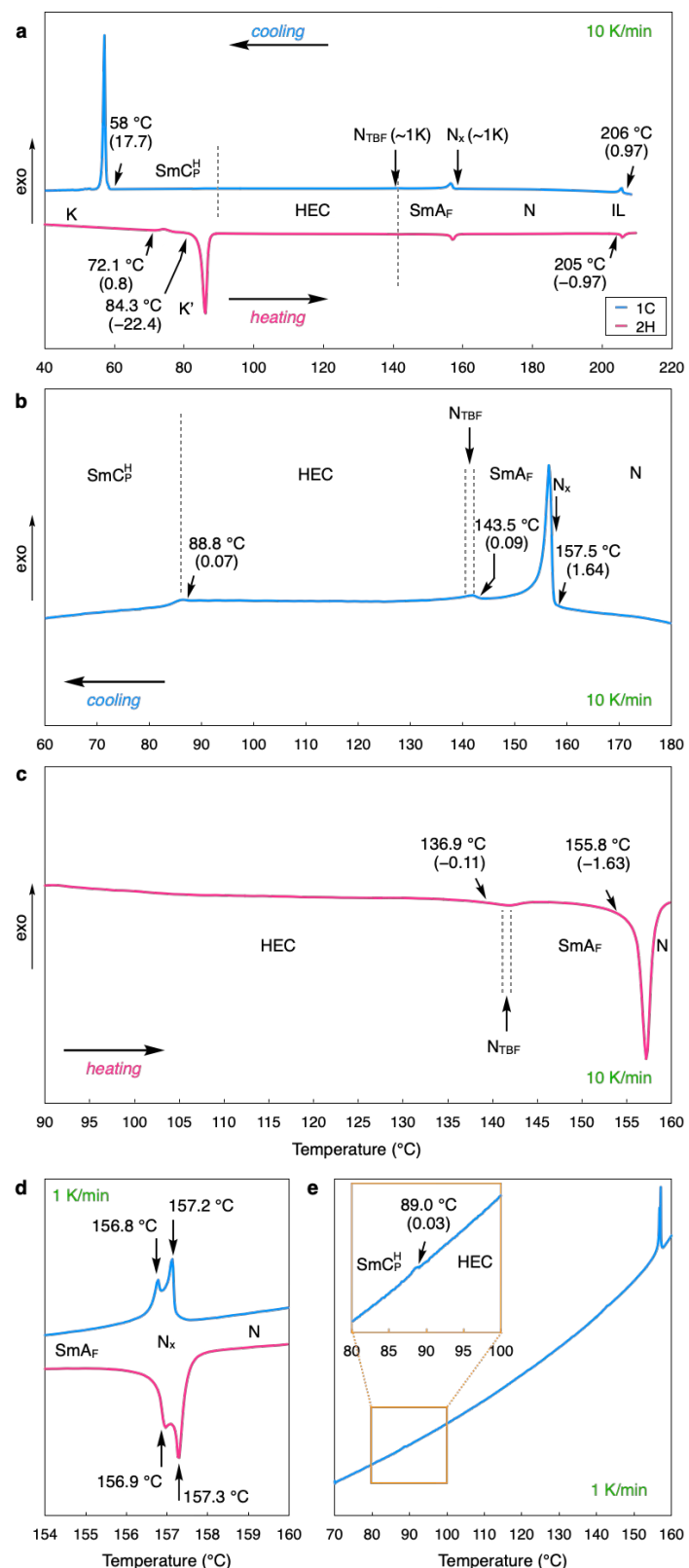


**Figure S1** DSC curves for Compound 1. Overall curves (a) and enlarged curves during cooling (b) and heating (c). Scan rate: 10 K min<sup>-1</sup>. d,e) DSC curves recorded at a scan rate of 1 K min<sup>-1</sup>.

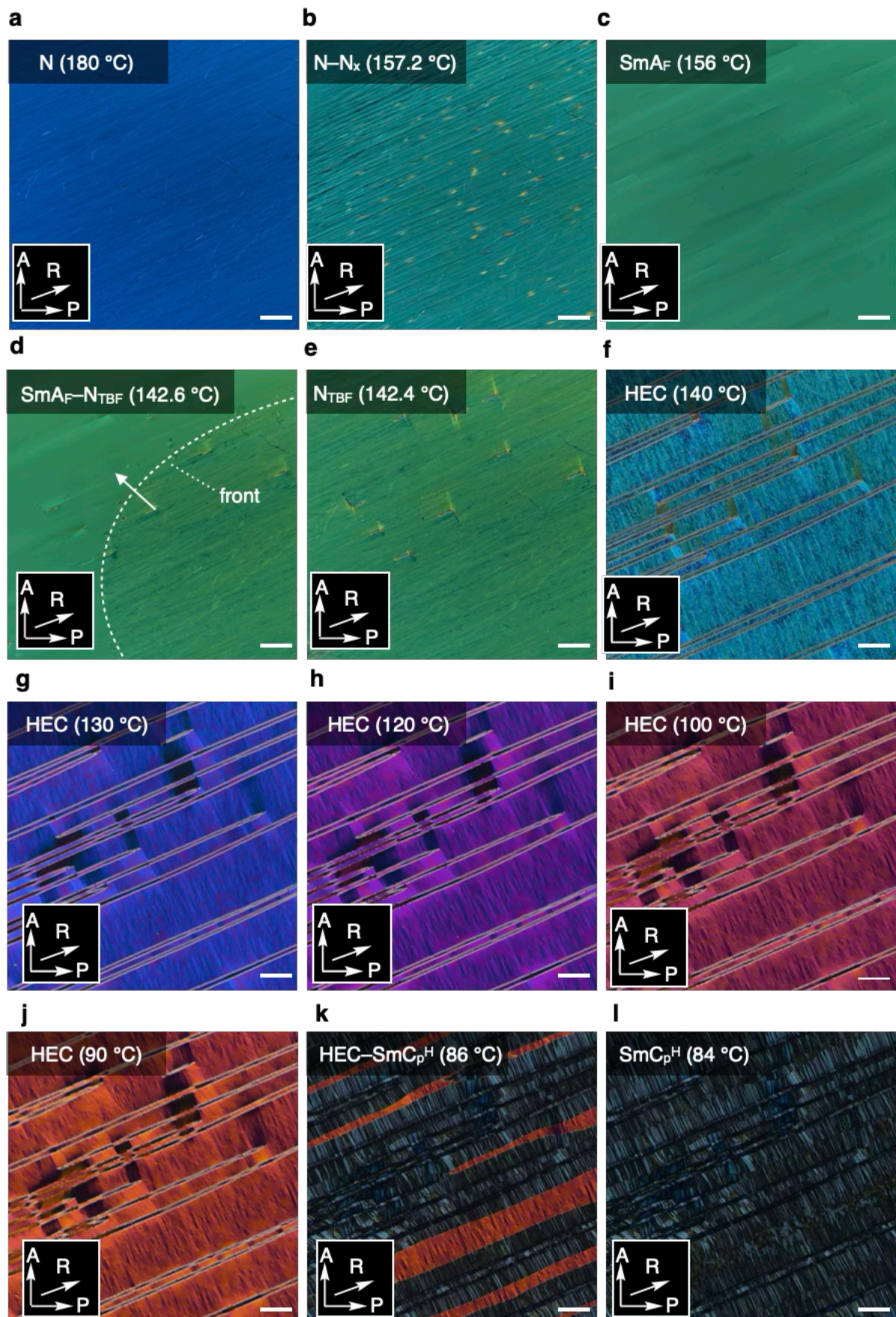


**Figure S2** Complete POM images taken in various temperature in SP cell (thickness: 5  $\mu\text{m}$ ) for Compound **1**. Scale bar: 100  $\mu\text{m}$ .

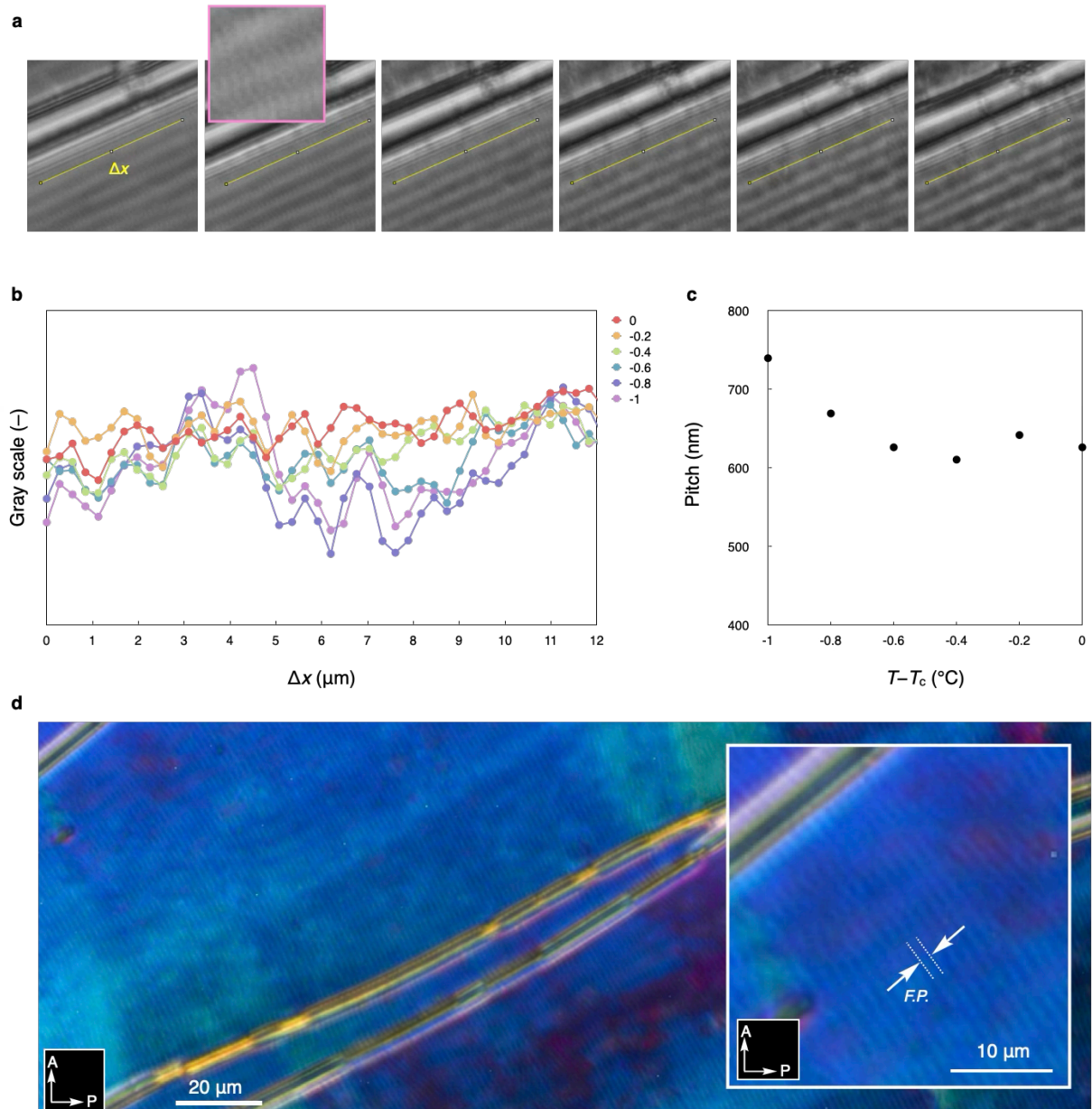


**Figure S3** Image analysis to estimate helical pitch in the  $N_{TBF}$  range. a) 8-bit POM images, b) cross-sectional intensity profile perpendicular to fine stripes, c) estimated pitch vs temperature. d) POM image taken in the cover glass substrate cell without alignment layer and spacers. Similarly, the full pitch  $\approx 1.3 \mu\text{m}$  was estimated.

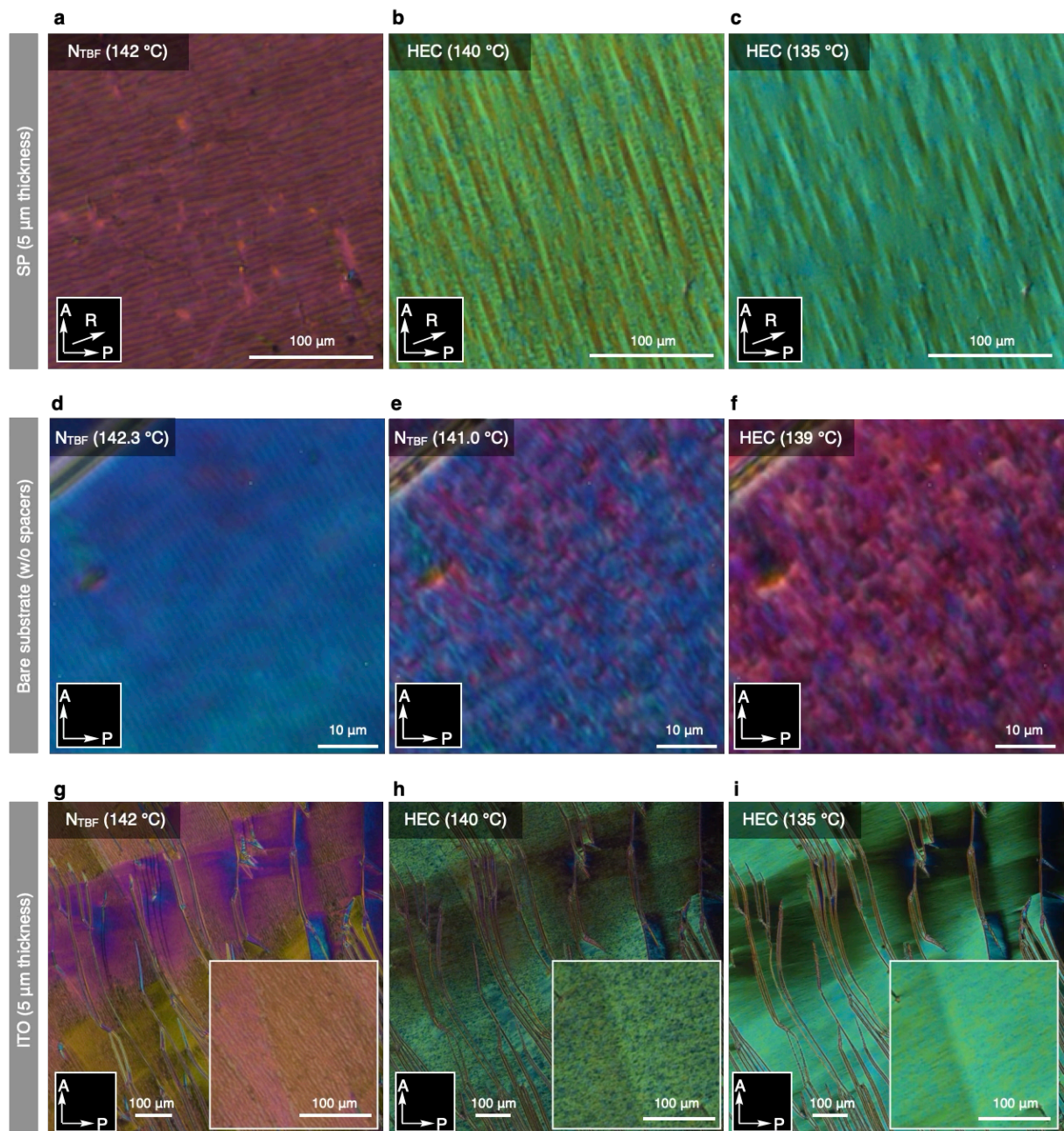


**Figure S4** Changes in POM texture taken in various temperature in SP (another lot) (a–c), bare substrate without spacers (d–f) and ITO cells (g–h) for Compound **1**. Thickness: SP cell, 5.0  $\mu$ m; ITO cell, 5.0  $\mu$ m.

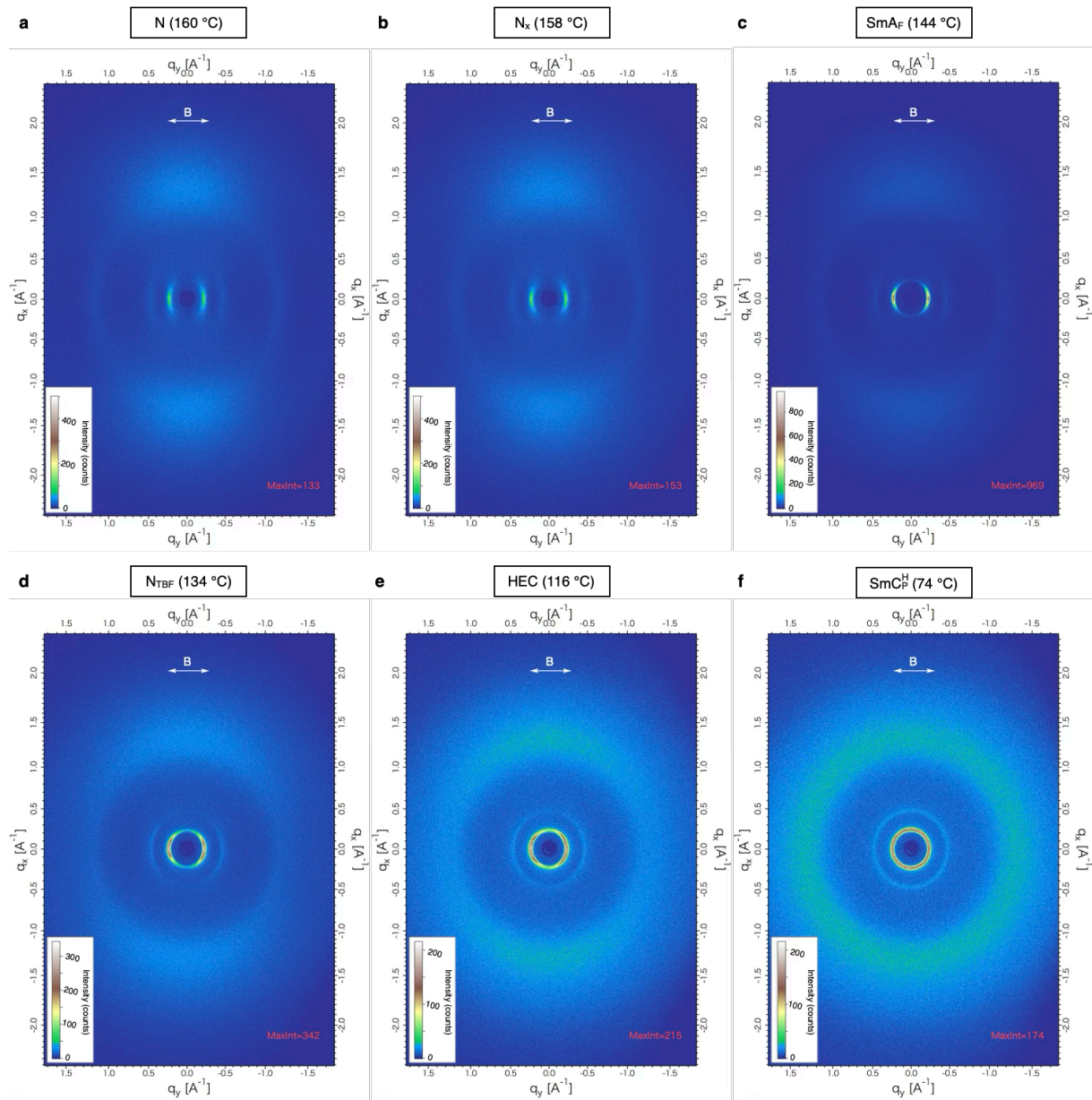


**Figure S5** Full-range 2D WAXD patterns in various phases under the magnetic field ( $\sim 1$  T,  $\mathbf{B} \parallel \mathbf{n}$ ) for Compound 1.

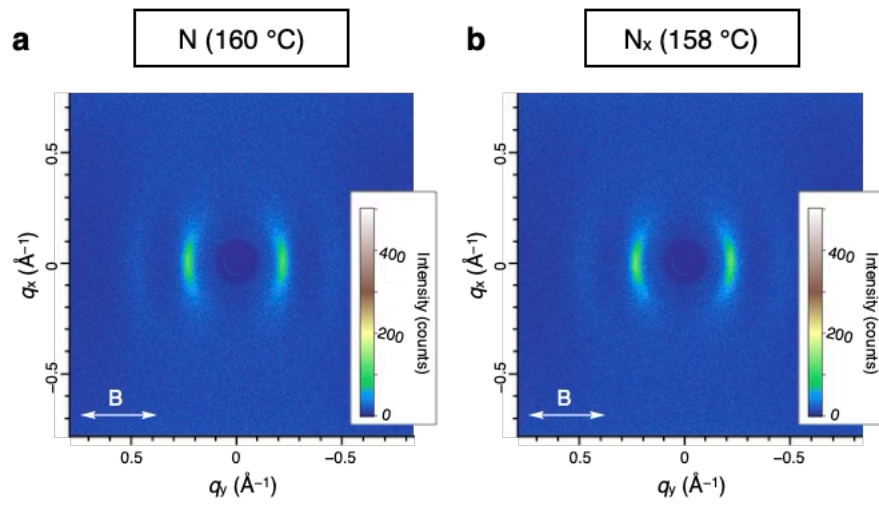


**Figure S6** 2D WAXD patterns in the N (a) and Nx (b) phase under the magnetic field ( $\sim 1$  T,  $\mathbf{B} \parallel \mathbf{n}$ ) for Compound 1.

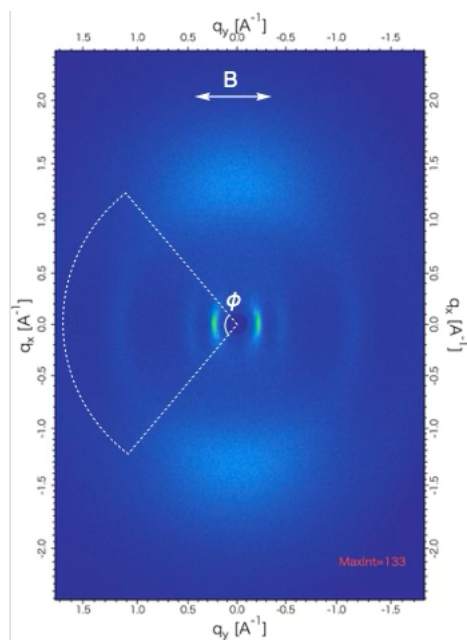


**Figure S7** Box scan area ( $\phi = 100^\circ$ ) on 2D X-ray pattern for generating 1D X-ray diffractogram.

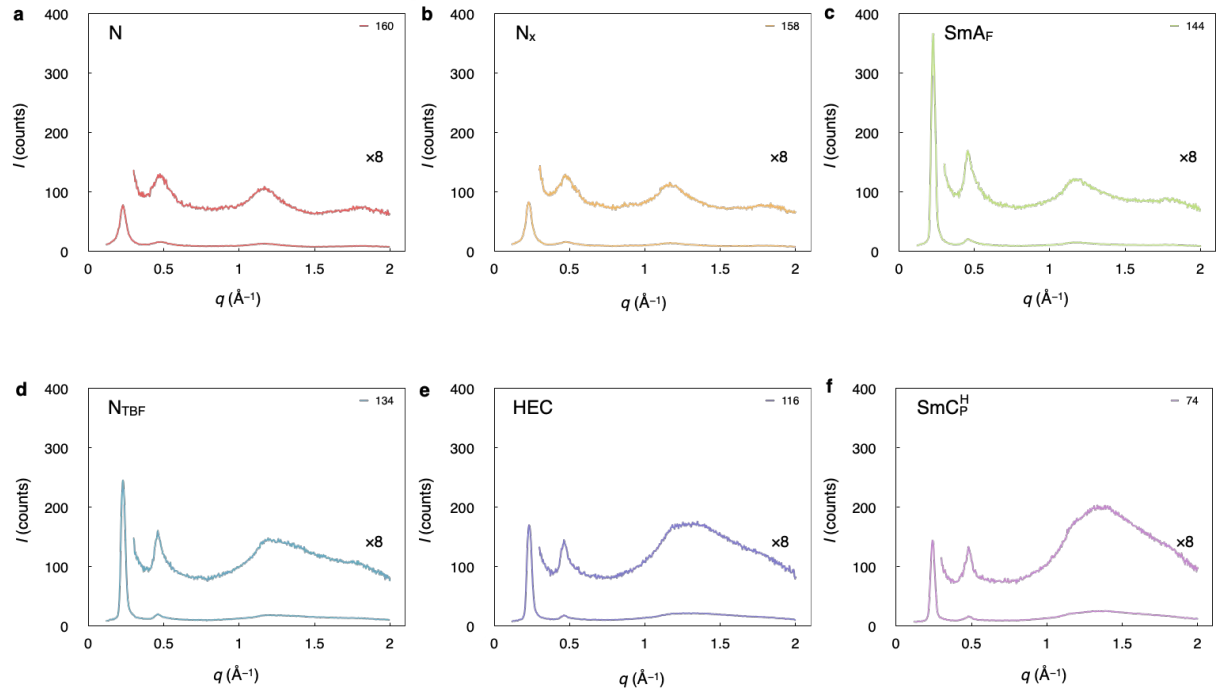


**Figure S8** 1D X-ray diffractogram along the equator direction ( $\mathbf{n} \parallel \mathbf{B}$ ) from a box scan area ( $\phi = 100^\circ$ ).

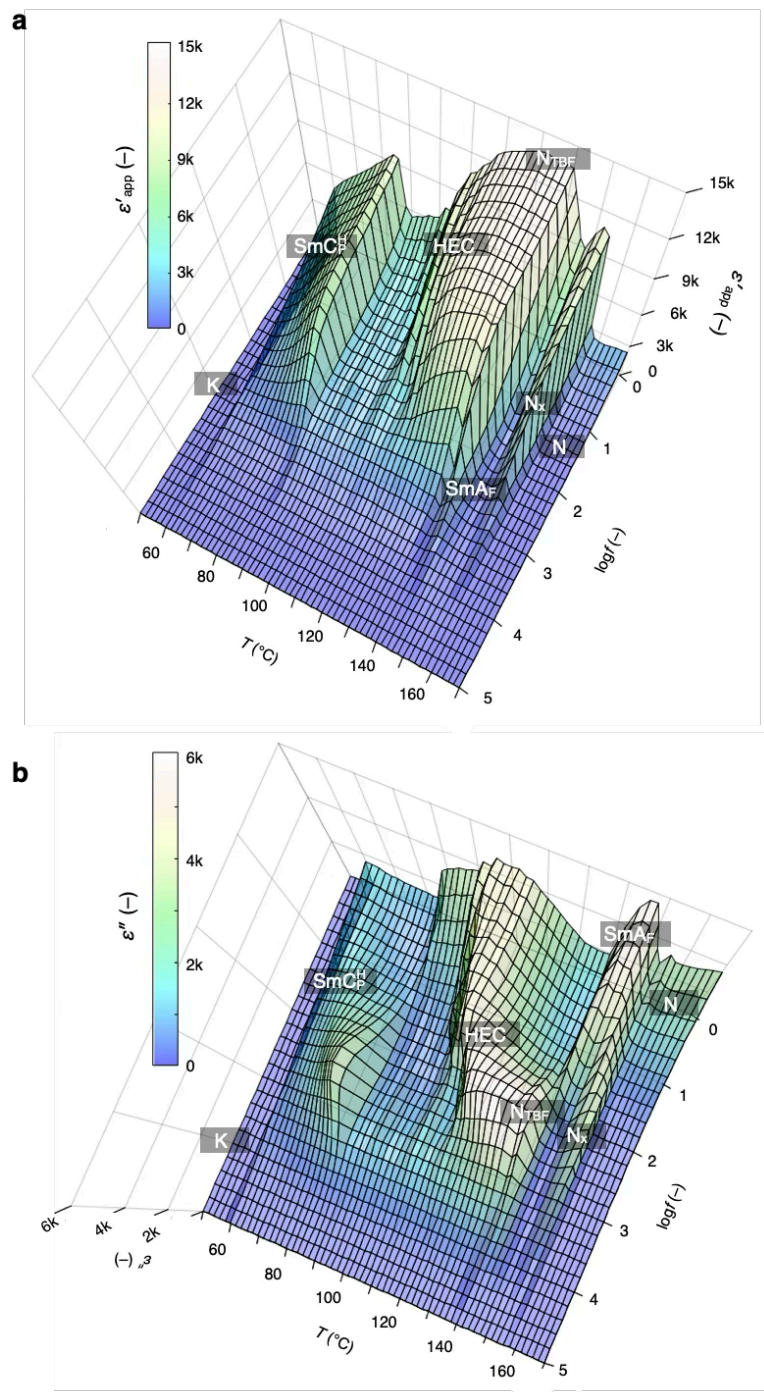


**Figure S9** 3D BDS data for Compound **1** in various temperatures. (a) Apparent dielectric permittivity vs  $\log f$ , Temperature; (b) dielectric loss vs  $\log f$ , Temperature.

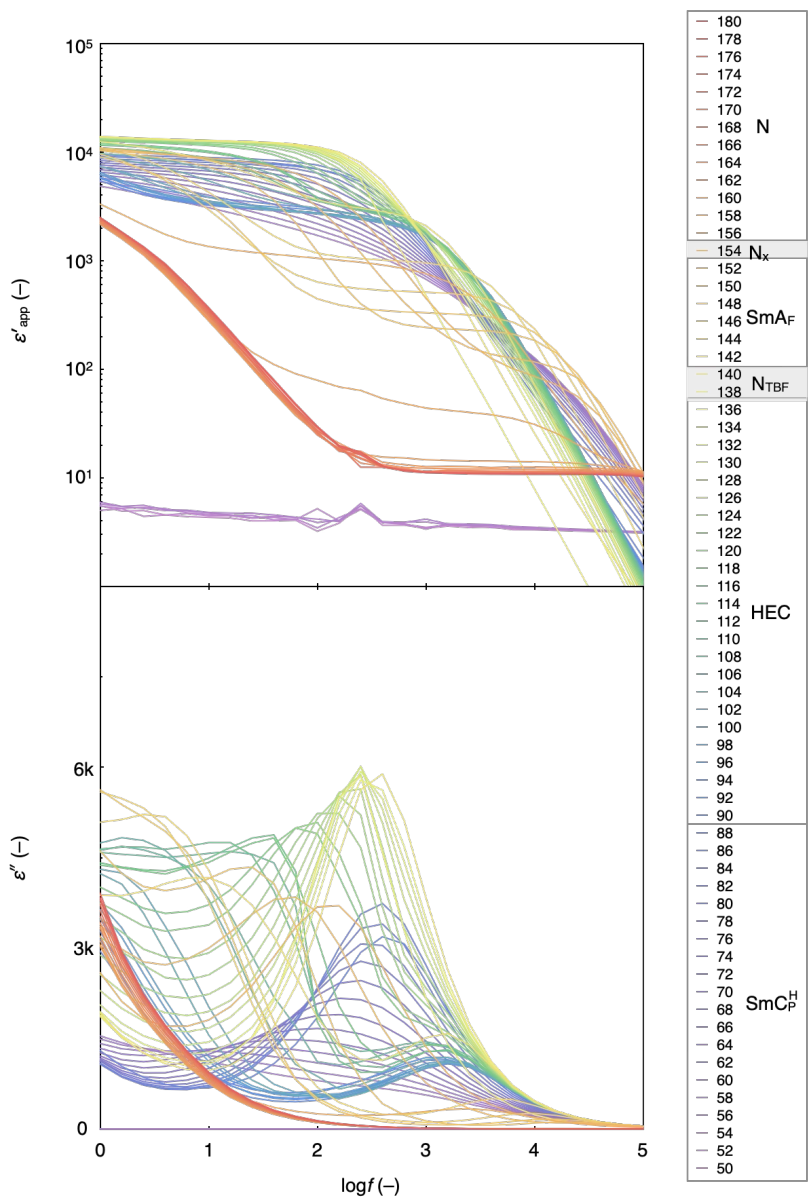


**Figure S10** Complete BDS data for Compound 1 in various temperatures.

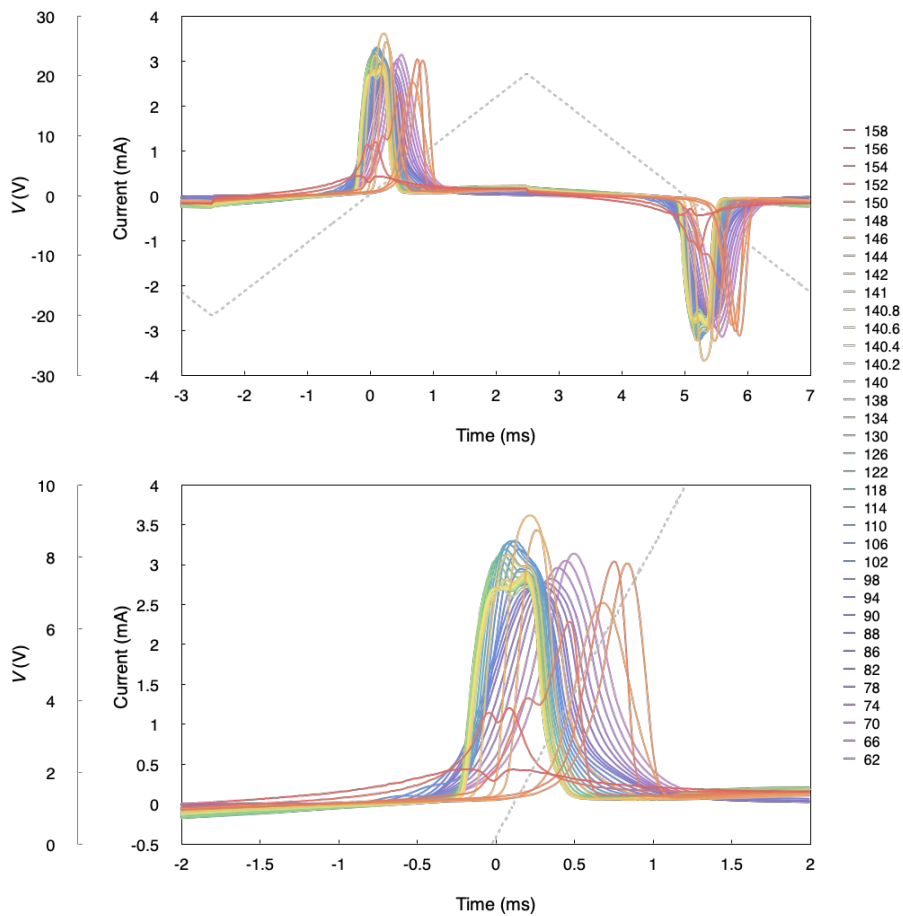


**Figure S11** Complete PRC data in various temperatures for Compound 1. Overall profile (a) and enlarged one (b).

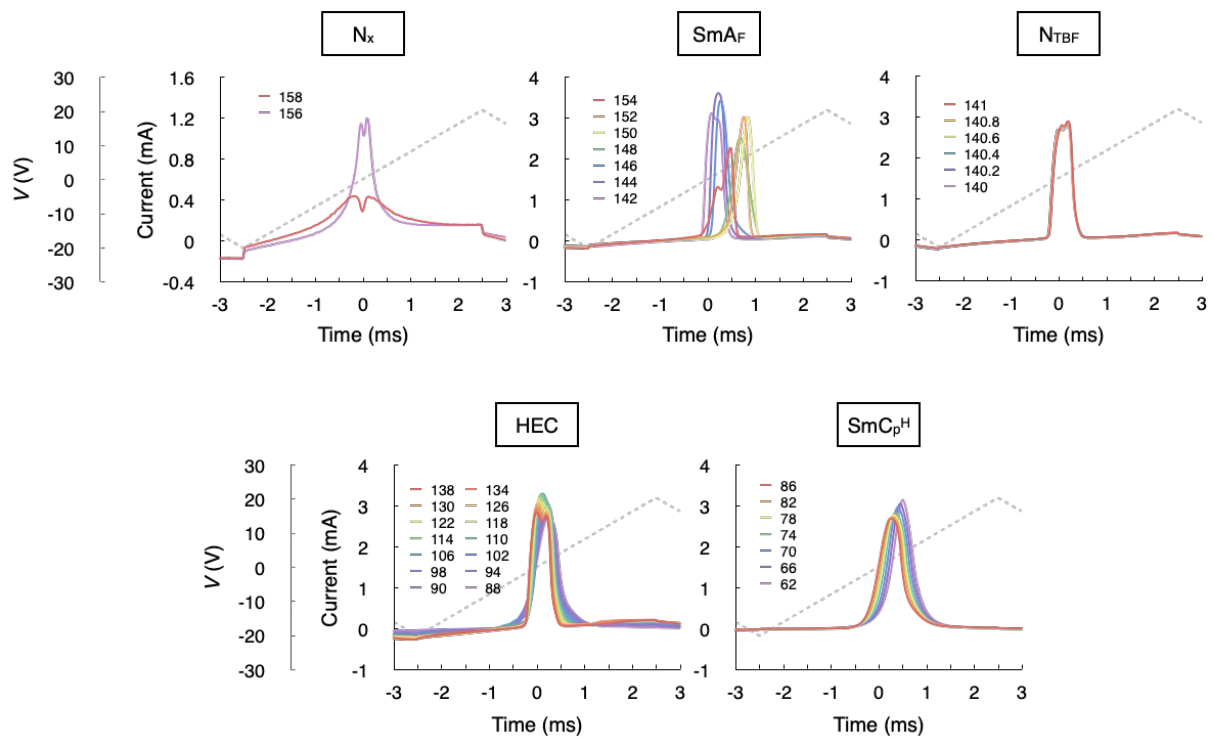


**Figure S12** Complete PRC data with applied voltage profile in various LC regions for Compound 1.

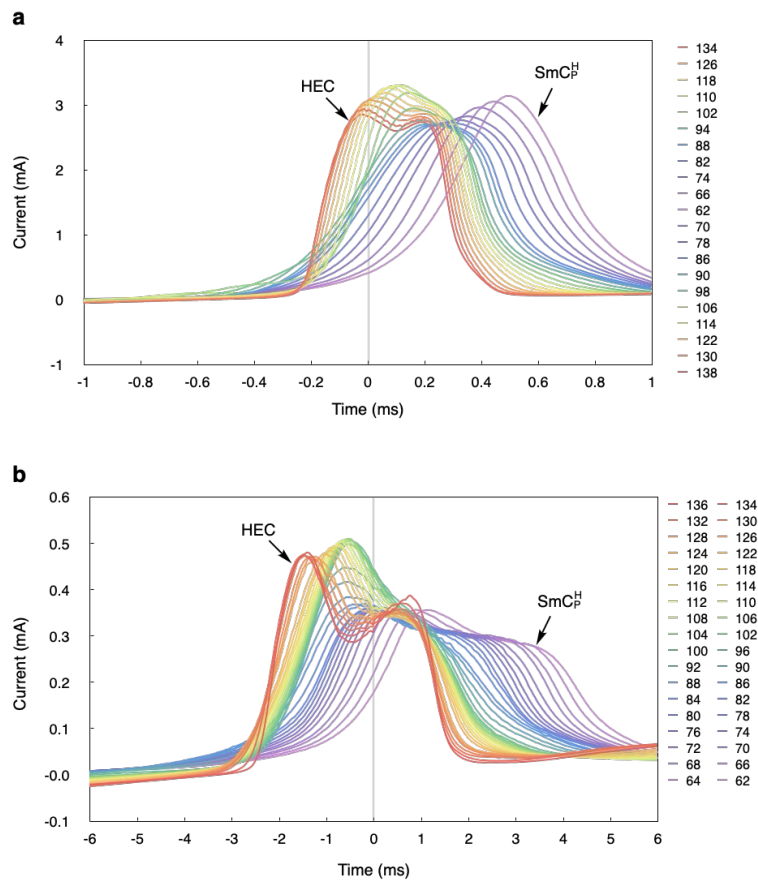


**Figure S13** Comparison of PRC data within HEC and  $\text{SmC}_\text{P}^\text{H}$  ranges for Compound 1. PRC data obtained under conditions: (a)  $V_{\text{pp}} = 40 \text{ V}, f = 100 \text{ Hz}$  (b)  $V_{\text{pp}} = 20 \text{ V}, f = 20 \text{ Hz}$ .

## *Applying E-field*

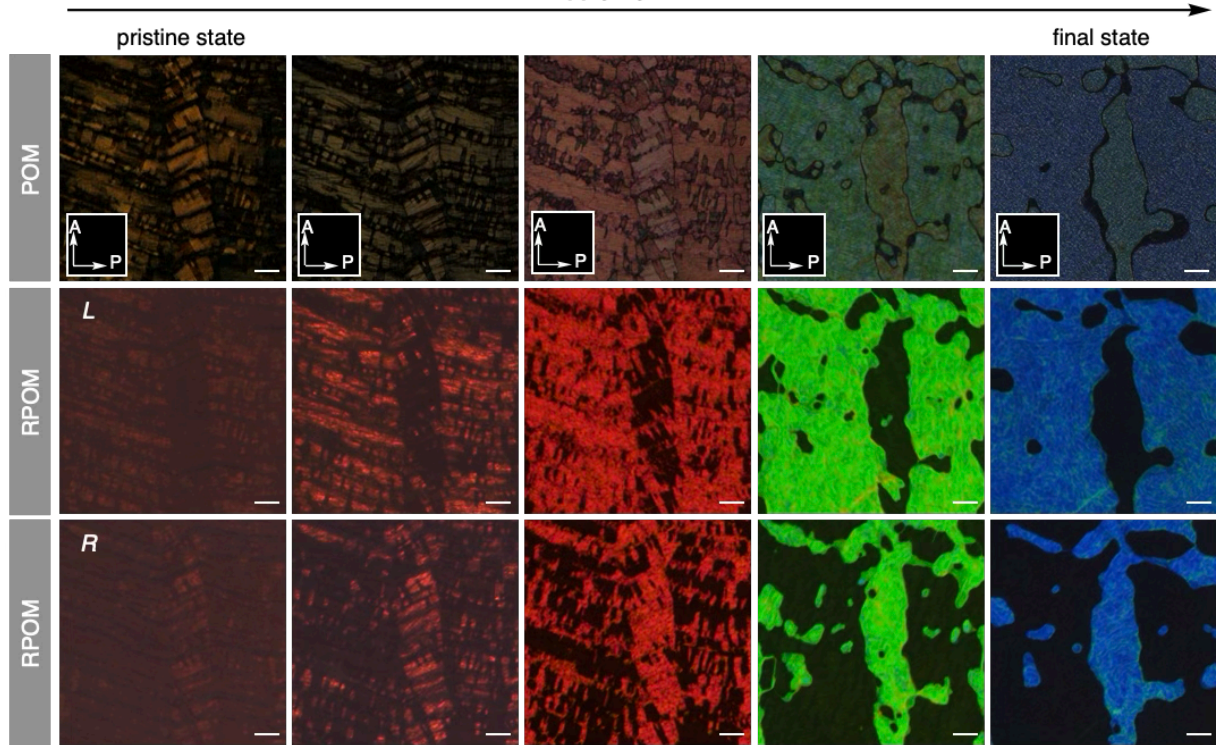


**Figure S14** Changes in POM and RPOM images in the SmC<sub>p</sub><sup>H</sup> phase (75 °C) under AC *E*-field.

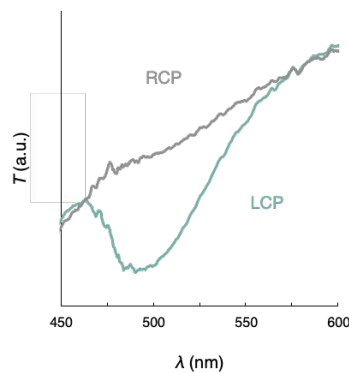


**Figure S15** Transmittance spectra at the local homochiral domain through right- and left-handed circular polarizers (RCP and LCP) in the  $\text{SmC}_\text{p}^\text{H}$  phase (75 °C) under  $E$ -field.

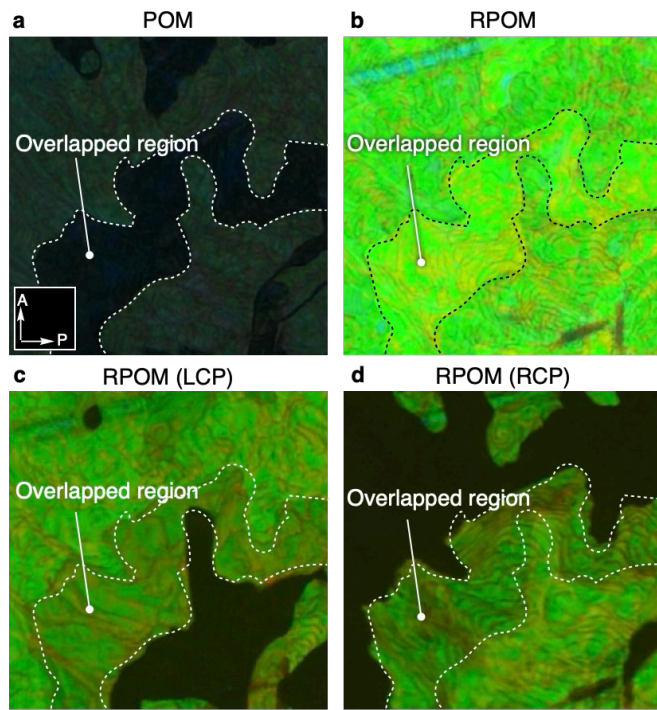


**Figure S16** Extend POM images in the  $\text{SmC}_\text{P}^{\text{H}}$  phase (75 °C) under  $E$ -field. a) POM, b) reflective mode POM (RPOM) and RPOM images through left- (c) and right- (d) handed circular polarizers.

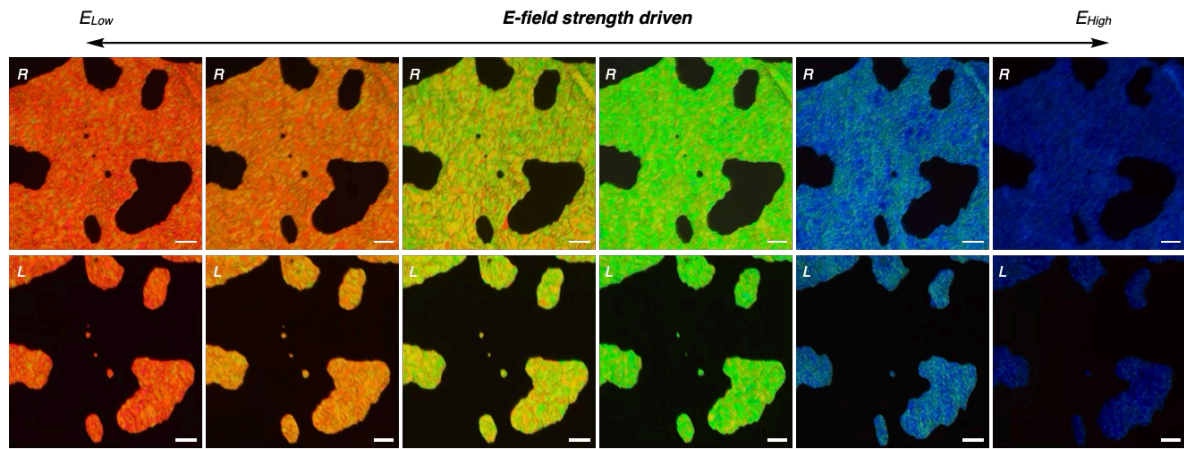


**Figure S17** Extend RPOM images of the  $\text{SmC}_\text{P}^\text{H}$  phase ( $75^\circ\text{C}$ ) under  $E$ -field. These images were taken in thin LC cell ( $4.5\ \mu\text{m}$ ) through LCP and PRC.

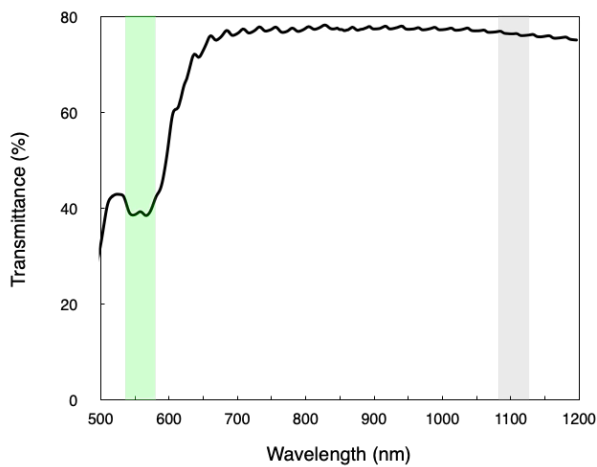


**Figure S18** UV-Vis-NIR spectra recorded in the SmC<sub>P</sub><sup>H</sup> phase (75 °C) for Compound **1** under *E*-field of 0.75 V<sub>pp</sub> μm<sup>-1</sup>.

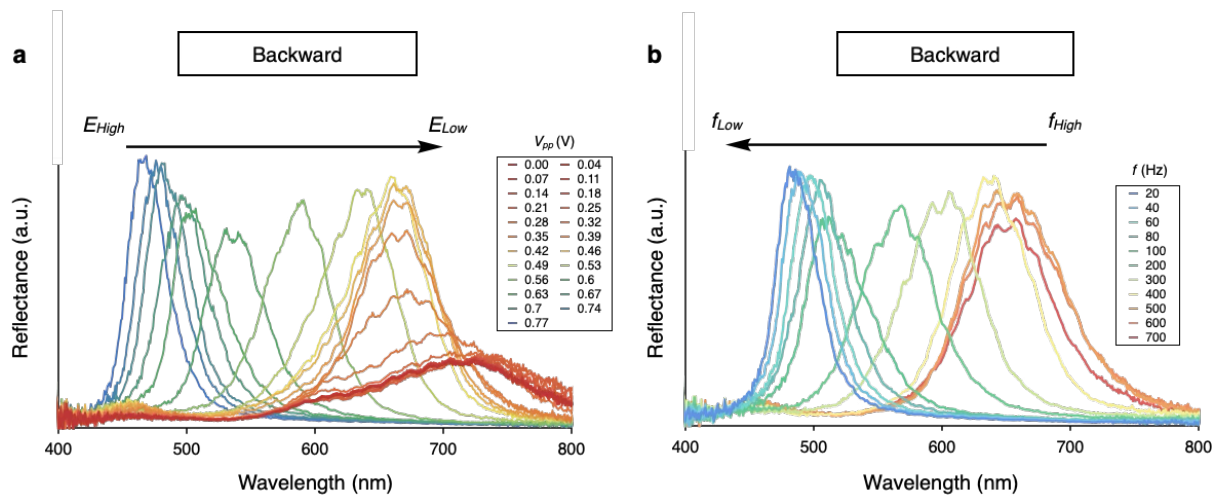


**Figure S19** Backward process of  $E$ -field- (a) and Frequency- (b) driven modulation for reflection band in the  $\text{SmC}_\text{P}^{\text{H}}$  phase ( $75^\circ\text{C}$ ): (a)  $E_{\text{High}}$  to  $E_{\text{low}}$ , (b)  $f_{\text{High}}$  to  $f_{\text{Low}}$ .

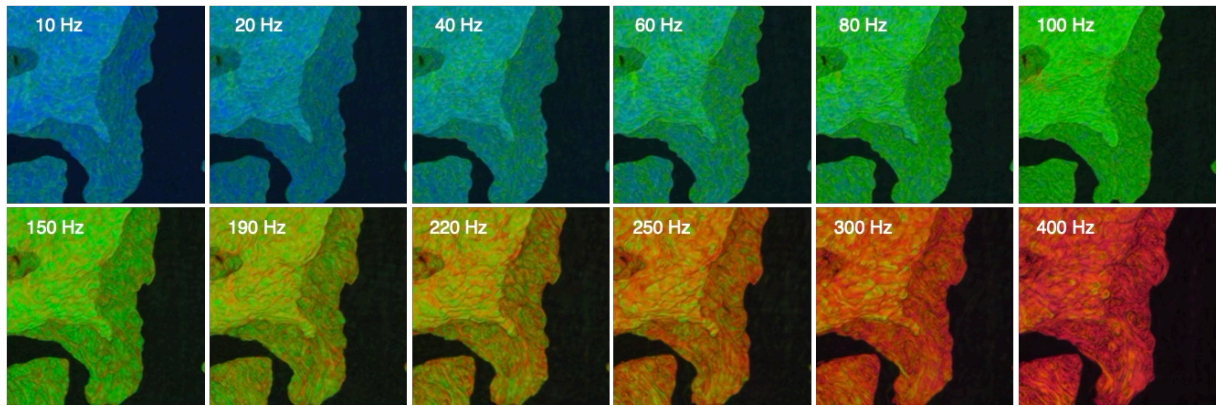


**Figure S20** Frequency-dependent RPOM images ( $f = 10\text{--}400\text{ Hz}$ ) taken through the RCP in the  $\text{SmC}_\text{P}^\text{H}$  phase ( $75\text{ }^\circ\text{C}$ ) under fixed  $E$ -field (square waveform,  $9.0\text{ V}_\text{pp}$ ).

Conventional	Polar alternative (from 2024)	
heliconical nematic	heliconical ferroelectric nematic ( $\text{N}_{\text{TBF}}\text{H}^{\text{C}}\text{N}_\text{F}$ )	This work polar heliconical smectic C ( $\text{SmCP}^{\text{H}}$ )
Components		
Complex $\left( \begin{array}{l} \text{rod-like molecule} \\ + \\ \text{dimeric molecule} \\ + \\ \text{chiral dopant} \end{array} \right)$	Simple $\left( \begin{array}{l} \text{single polar} \\ \text{rod-like molecule} \end{array} \right)$	
Properties		
Alignment layer	Need	Needless
$P_s$	–	$4\text{--}6 \text{ } (\mu\text{C}/\text{cm}^2)$
$E_{\text{AC}}$ (red $\rightleftharpoons$ blue)	$0.79\text{--}1.02 \text{ } (\text{V } \mu\text{m}^{-1})$	–
$E_{\text{DC}}$ (red $\rightleftharpoons$ blue)	–	$0.35\text{--}0.75 \text{ } (\text{V } \mu\text{m}^{-1})$
$f$ (red $\rightleftharpoons$ blue)	$73.5\text{--}1 \text{ (kHz)}$	–
Functionalities		
Multicolor modulation by $ E $ and $f$	✓	✓ (This work)
Tunable SHG	Complicated	✓ (This work)

**Figure S21** Comparison of key material characteristics between nonpolar and polar heliconical superstructures.

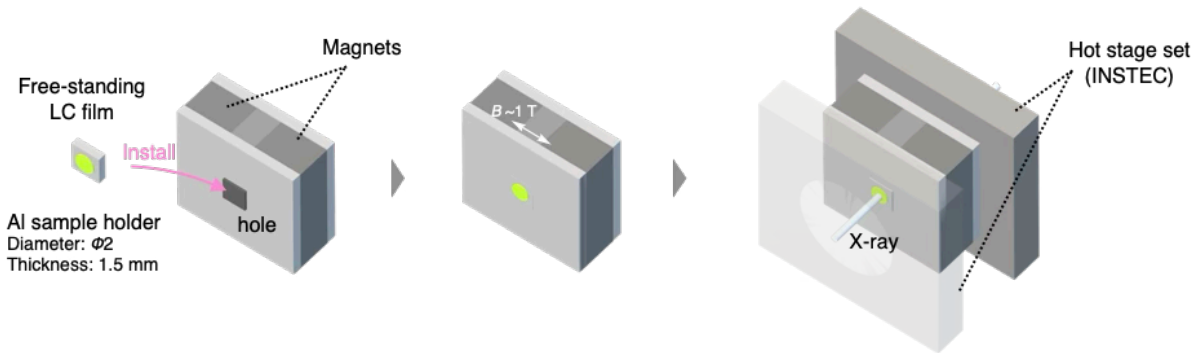


**Figure S22** Measurement setup for XRD studies under magnetic field.

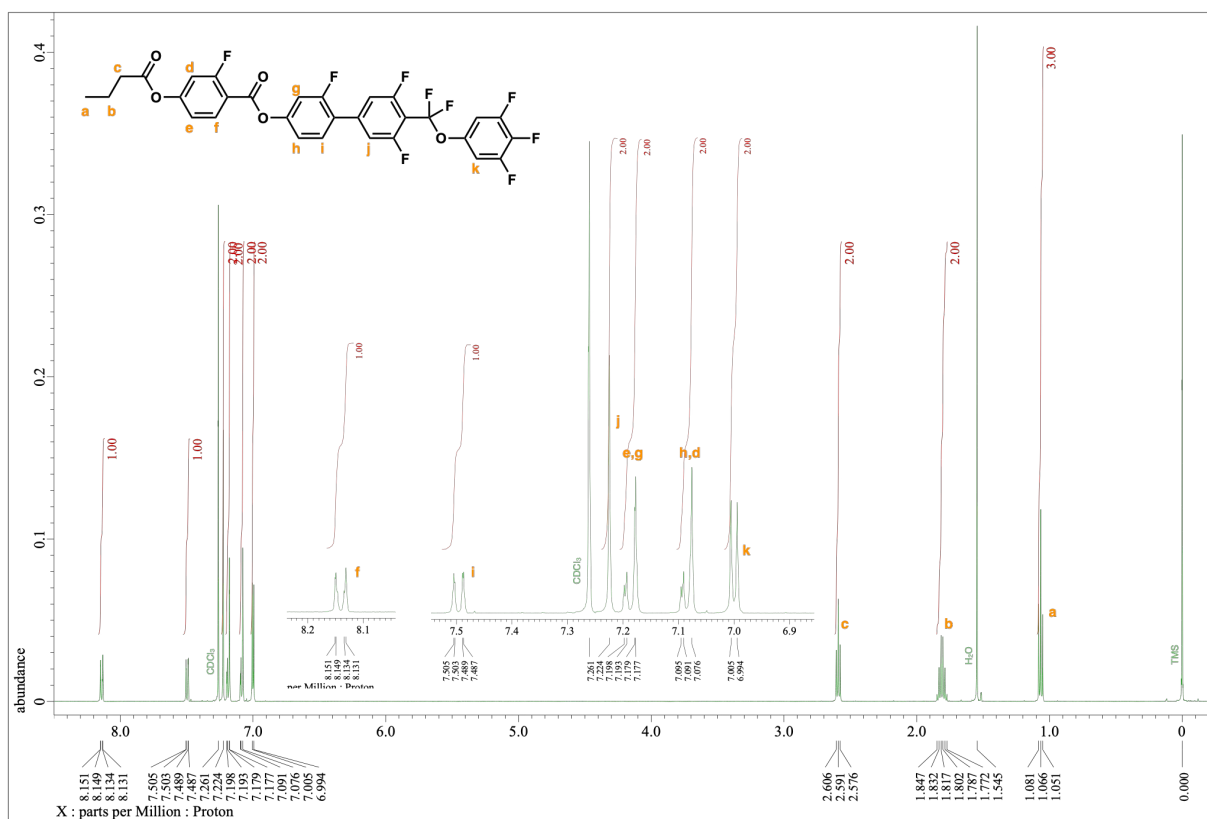


**Figure S23**  $^1\text{H}\{^{19}\text{F}\}$ NMR spectra for Compound **1**.

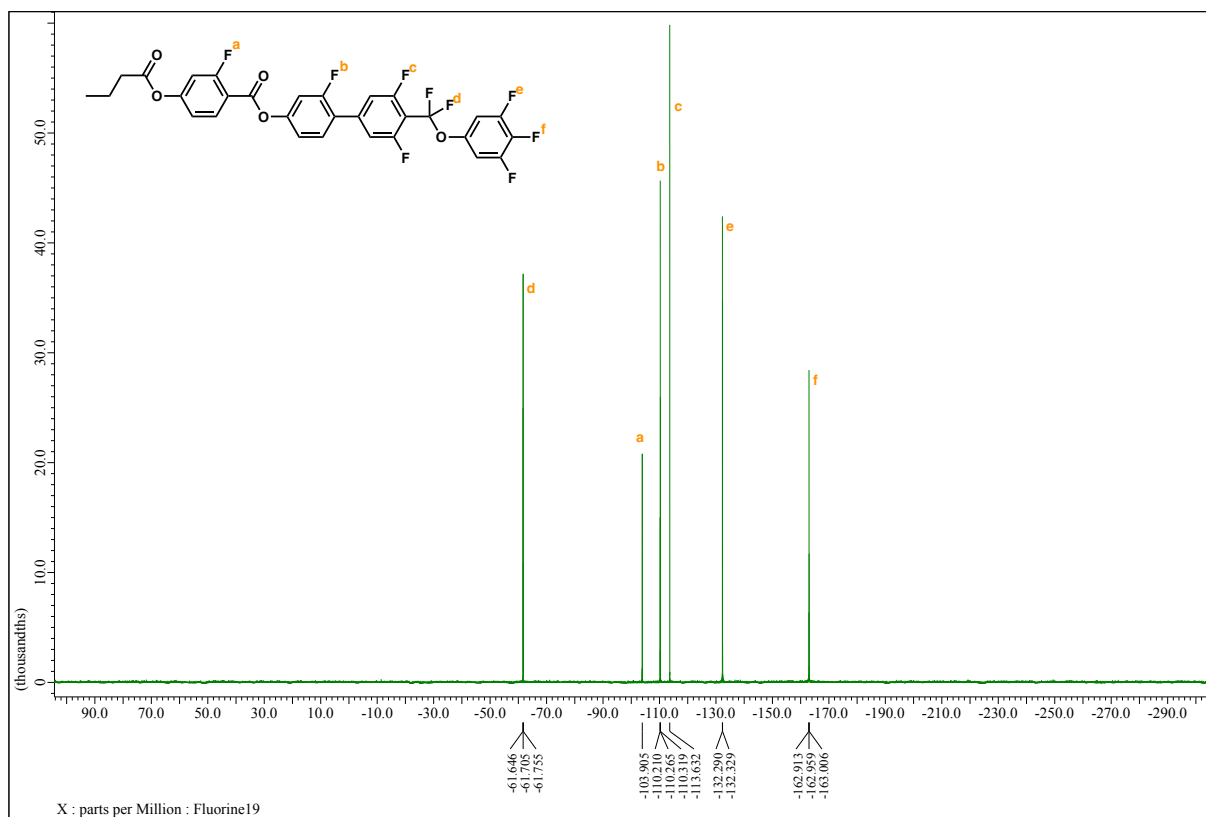


**Figure S24**  $^{19}\text{F}\{^1\text{H}\}\text{NMR}$  spectra for Compound 1.

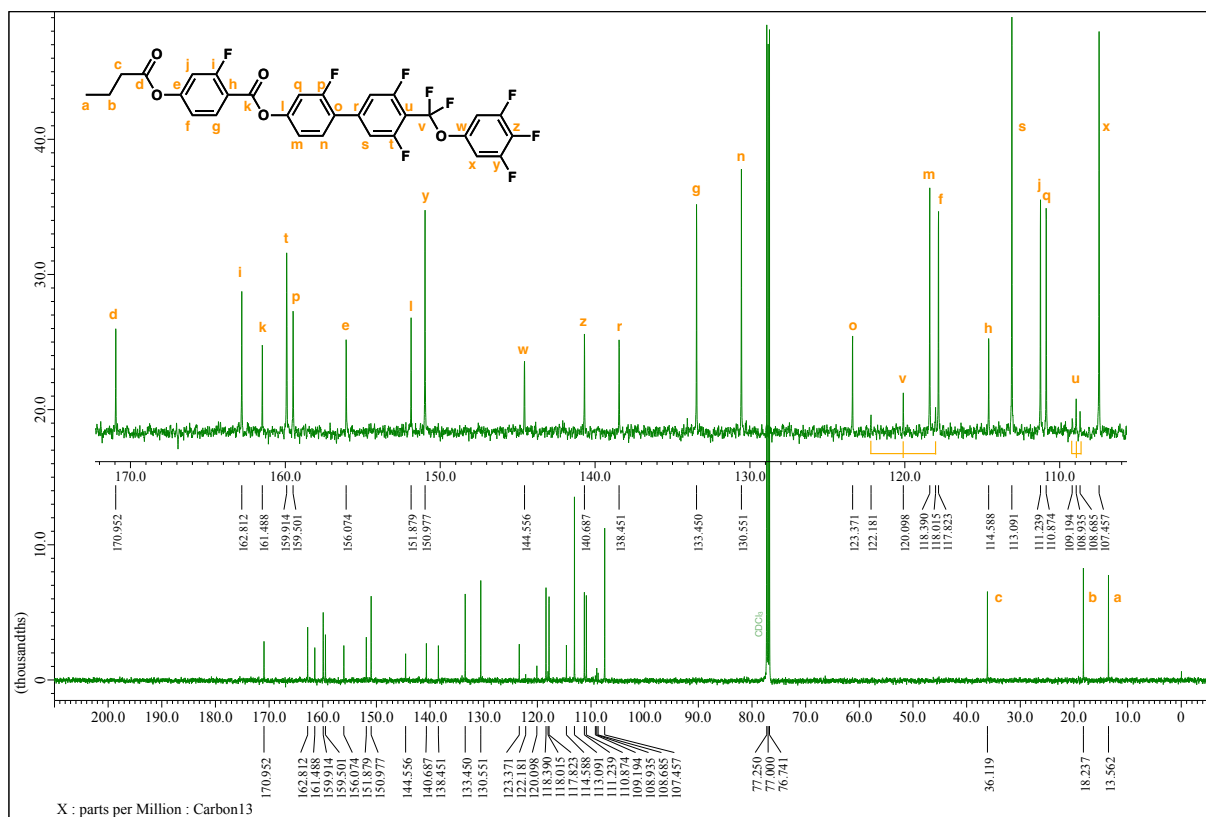


**Figure S25**  $^{13}\text{C}\{^{1}\text{H},^{19}\text{F}\}$ NMR spectra for Compound 1.

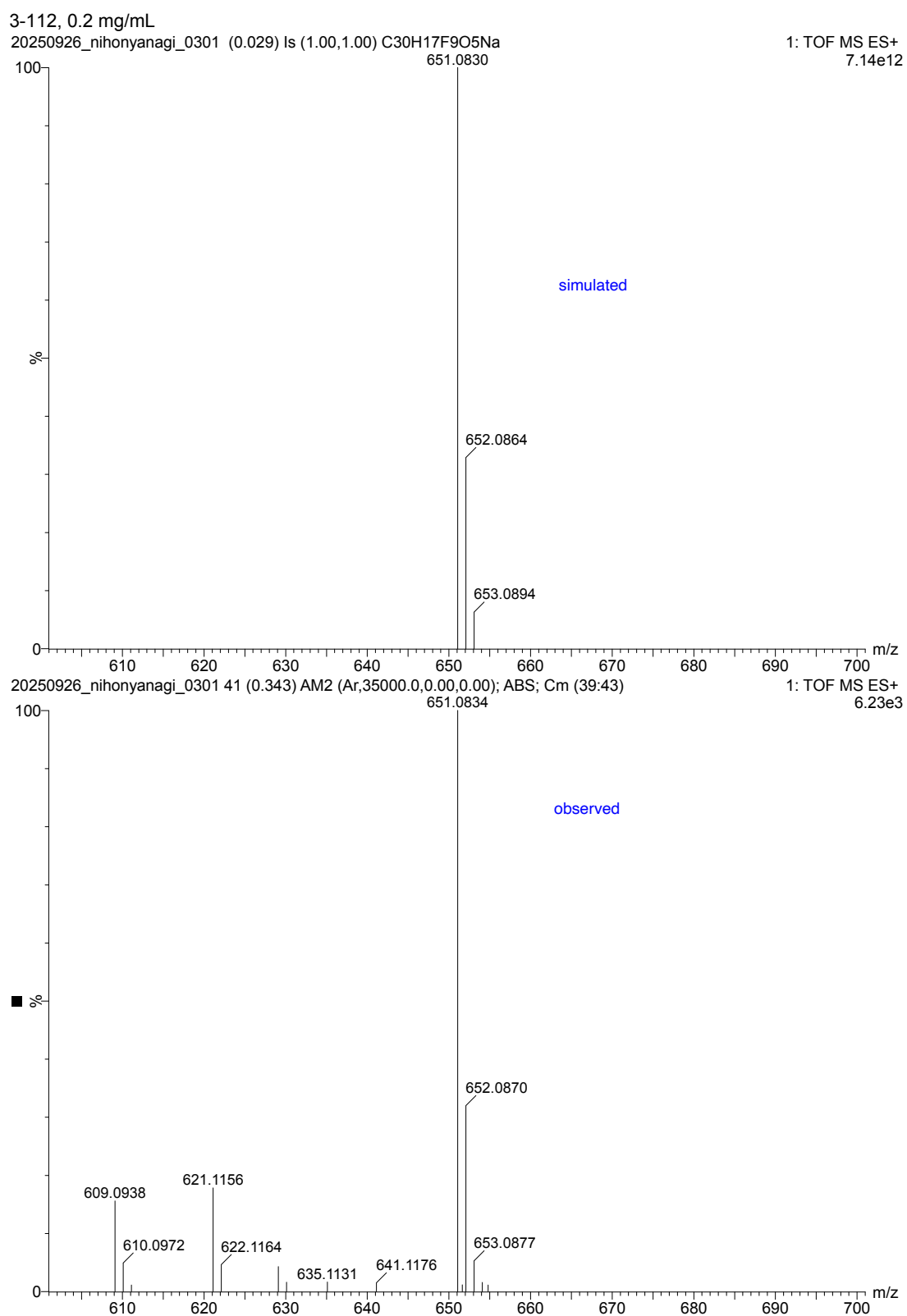


**Figure S26** HRMS spectra for Compound 1.

## Supplementary Tables (Table S1, S2)

**Supplementary Table 1** | The molecular parameters of energy-minimized conformations calculated by DFT for Compound 1.

Entry	Vector X	Vector Y	Vector Z	$\mu$ (D)	$\beta$ (deg) <sup>†</sup>
<b>Compound 1</b>	10.0869	-4.1888	-1.8005	11.07	24.32

† An angle between the permanent dipole moment ( $\mu$ ) and long molecular axis.

**Table S2** | Phase transition temperature (°C) and enthalpy changes (kJ mol<sup>-1</sup>, in parentheses) for Compound **1**. Rate: 10 K min<sup>-1</sup> and 1 K min<sup>-1</sup>.

Process	K	SmC <sub>p</sub> <sup>H</sup>	HEC	N <sub>TBF</sub>	SmA <sub>F</sub>	N <sub>x</sub>	N	IL
1C	•	58.0 (17.7)	•	88.8 (0.07) (0.03) <sup>b</sup>	• Xxx <sup>a</sup> (i)	• 143.0 <sup>a</sup> (ii)	• 156.8 <sup>a,b,c</sup> (iii)	• 157.2 <sup>a,b,c</sup> (iv)
2H	•	84.3 (-22.4)	—	—	• 136.9 <sup>a</sup> (v)	• — <sup>d</sup> (vi)	• 156.9 <sup>a,b,c</sup> (vii)	• 157.3 <sup>a,b,c</sup> (viii)

<sup>a</sup> Overlapping peaks on DSC trace, temperature taken from POM and/or DSC. i + ii = 0.05 kJ mol<sup>-1</sup>, iii + iv = 1.17 kJ mol<sup>-1</sup>, v + vi = -0.05 kJ mol<sup>-1</sup>, vii + viii = -0.145 kJ mol<sup>-1</sup>. <sup>b</sup> Rate: 1 K min<sup>-1</sup>. <sup>c</sup>  $T_{peak-top}$ . <sup>d</sup> Undeterminable.

## Supplementary Videos (Video S1)

**Video S1** | Multicolor modulation in the  $\text{SmC}_\text{P}^\text{H}$  phase of Compound **1** (75 °C). Conditions: ITO glass cell (gap: 14.1  $\mu\text{m}^{-1}$ ), frequency: 100 Hz, *E*-field (square waveform): 0 to 11 V<sub>pp</sub>.

**Video S2** | Multicolor modulation in the  $\text{SmC}_\text{P}^\text{H}$  phase of Compound **1** (75 °C). Conditions: ITO glass cell (gap: 14.1  $\mu\text{m}^{-1}$ ), frequency: 100 Hz, *E*-field (square waveform): 11 to 0 V<sub>pp</sub>.

**Video S3** | Multicolor modulation in the  $\text{SmC}_\text{P}^\text{H}$  phase of Compound **1** (75 °C). Conditions: ITO glass cell (gap: 14.1  $\mu\text{m}^{-1}$ ), *E*-field (square waveform): 9 V<sub>pp</sub>, frequency: 10 to 400 Hz.

**Video S3** | Multicolor modulation in the  $\text{SmC}_\text{P}^\text{H}$  phase of Compound **1** (75 °C). Conditions: ITO glass cell (gap: 14.1  $\mu\text{m}^{-1}$ ), *E*-field (square waveform): 9 V<sub>pp</sub>, frequency: 400 to 10 Hz.

**Video S4** | POM texture (reflective mode) recorded thorough a left-handed circular polarizer in the  $\text{SmC}_\text{P}^\text{H}$  phase of Compound **1** (75 °C). Conditions: ITO glass cell (gap: 14.1  $\mu\text{m}^{-1}$ ), *E*-field (square waveform): 11 V<sub>pp</sub>, frequency: 100 Hz.

**Video S5** | POM texture (reflective mode) recorded thorough a right-handed circular polarizer in the  $\text{SmC}_\text{P}^\text{H}$  phase of Compound **1** (75 °C). Conditions: ITO glass cell (gap: 14.1  $\mu\text{m}^{-1}$ ), *E*-field (square waveform): 11 V<sub>pp</sub>, frequency: 100 Hz.

## Supplementary References

S1 M. J. Frisch, G. W. Trucks, H. B. Schlegel, G. E. Scuseria, M. A. Robb, J. R. Cheeseman, G. Scalmani, V. Barone, B. Mennucci, G. A. Petersson, H. Nakatsuji, M. Caricato, X. Li, H. P. Hratchian, A. F. Izmaylov, J. Bloino, G. Zheng, J. L. Sonnenberg, M. Hada et al. Gaussian 09, revision E.01; Gaussian, Inc.: Wallingford, CT, (2009).

S2 H. Nishikawa et al. *Adv. Mater.* **2025**, e13451, <http://doi.org/10.1002/adma.202513451>.